THE JOURNAL OF PHYSICAL CHEMISTRY C
A JOURNAL OF THE AMERICAN CHEMICAL SOCIETY

pubs.acs.org/JPCC Article

In Situ XAFS, XRD, and DFT Characterization of the Sulfur Adsorption Sites on Cu and Ce Exchanged Y Zeolites

Henry J. Sokol, Amani M. Ebrahim, Stavros Caratzoulas, Anatoly I. Frenkel,* and Julia A. Valla*

Cite This: *J. Phys. Chem. C* 2022, 126, 1496−1512 Read Online

ACCESS | Metrics & More | Article Recommendations | Supporting Information

ABSTRACT: Adsorptive desulfurization with Cu and Ce ion-exchanged Y zeolite (CuCeY) has proven to be an effective method for the removal of sulfur compounds from hydrocarbon fuels. In this study, Cu and Ce exchanged Y materials including CuY, CeY, and CuCeY were prepared and examined to investigate the mechanism behind the superior sulfur adsorption and selectivity of CuCeY. In situ conditions were used to study the materials as prepared for optimal desulfurization. X-ray diffraction (XRD) confirmed the absence of large well-ordered crystalline phases from metallic or oxide Cu and Ce after the reduction of the samples. The oxidation states and local environments of Cu and Ce were determined using X-ray adsorption fine structure (XAFS) analysis and correlated to theoretical findings obtained from density functional theory (DFT) calculations. XAFS data indicate the successful reduction of Cu species to Cu^{+} and Cu^{0}, and Ce to Ce^{3+}. Analysis of XAFS spectra located Cu and Ce within the Y zeolite framework with Cu cations in the six-member ring sites and as small metallic Cu clusters. Ce cations were found to occupy both six-member ring and hexagonal prism sites. These results reveal the structure of CuCeY as prepared for desulfurization and provide insight into its superior sulfur adsorption performance.

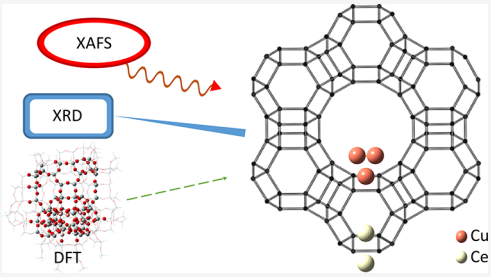

Downloaded via BROOKHAVEN NATL LABORATORY on January 27, 2022 at 21:28:37 (UTC).
See https://pubs.acs.org/sharingguidelines for options on how to legitimately share published articles.

1. INTRODUCTION

The removal of sulfur compounds from petroleum fuels is of great importance for a variety of environmental and human health reasons.[1] Especially in the transportation sector, many steps are taken to reduce the emission of harmful chemicals into the atmosphere. These include sulfur compounds present in fuels that can form sulfur oxides (SO_x) when combusted, leading to many negative environmental and public health effects.[2,3] In response to these concerns, the Environmental Protection Agency has mandated that sulfur levels should not exceed 15 ppm in diesel fuels and 10 ppm in gasoline.[4−6] All aforementioned measures are intended to improve air quality and public health but pose challenges to reduce the high sulfur content of petroleum sources to acceptable levels. In addition to the transportation sector, low sulfur fuels are necessary to avoid catalyst poisoning and deactivation of fuel cells.[7] For these applications, near zero sulfur levels are required to prevent performance degradation.[8]

Currently, the common method for sulfur reduction of transportation fuels is hydrodesulfurization (HDS).[9] HDS relies on high temperature and H_2 pressure to break down sulfur molecules in liquid fuels, a process that is cost and energy intensive and can lead to the deterioration of the fuel quality.[10] These issues can be avoided by adsorptive desulfurization (ADS), which can operate at ambient conditions to achieve near zero sulfur fuel.[11−13] Y zeolite has shown to be an effective adsorbent for thiophenic sulfur compounds.[14] Y zeolite has a porous faujasite (FAU) structure with large 7.4 Å pore openings to the supercage, allowing easy transport of adsorbate molecules.[15] In addition, the large surface area and availability of Brønsted acid sites provide active sites for adsorption of target molecules.[16] Metal ion exchange of various transition and rare earth (RE) metals has been used to increase the capacity and selectivity for sulfur compounds in the presence of competing adsorbates.[17,18] Specifically, the introduction of both Cu and Ce into the Y zeolite has shown superior sulfur adsorption properties due to synergistic interactions between the two metal species.[19,20] The bimetallic CuCeY zeolite has shown the high sulfur capacity exhibited by CuY and the strong selectivity of CeY for the adsorption of thiophene and benzothiophene (BT).[21,22] Sulfur adsorption has been found to occur on both metal cations in the zeolite active sites and metals within the supercage.[23] In our previous studies, we have demonstrated that the introduction of mesoporosity has been used to overcome diffusion limitations for the adsorption of larger sulfur compounds such as dibenzothiophene (DBT) and 4,6-dimethyldibenzothiophene (4,6-DMDBT).[20,24] Another advantage of the ADS process is that adsorbents have shown reusability with only a slight loss of sulfur capacity after

Received: October 20, 2021
Revised: December 14, 2021
Published: January 13, 2022

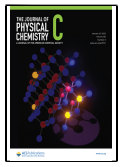

© 2022 American Chemical Society

https://doi.org/10.1021/acs.jpcc.1c09128
J. Phys. Chem. C 2022, 126, 1496−1512

regeneration.[25] Sulfur capacity has been restored using a high-temperature regeneration process and a solvent with similar polarity to the adsorbate.[26] In CuY, recovery of over 90% of sulfur capacity through regeneration has been demonstrated.[27]

While significant work has been done to show the superior sulfur adsorption of ion-exchanged Y zeolites, the exact structure and topology of exchanged metals are still being investigated. Thus, several different possibilities for the exact location of metals in ion-exchanged Y have been presented. Transition metals have been found into zeolites as isolated nanoclusters, cations, or oxide centers covalently bonded to the zeolite and as atoms incorporated into the framework.[28,29] Previous studies have shown Cu species in Y zeolite as Cu−Cu dimers; Cu^+ cations in sites I′, II′, and II; small Cu metal clusters; and small CuO clusters.[30−34] The placement of Cu cations in the active sites of Y zeolites has also varied, with another study finding Cu preferentially occupying sites I′, II, and III′.[35] Ce species have been found to be located as cations in the Y zeolite active sites as well as in the supercage. After liquid ion exchange with HY, Ce has been reported in sites I′ and II′.[36] Recent work has shown the fabrication of Ce active sites for sulfur adsorption in the supercages of CeY materials.[37] This current study investigates the placement of Cu and Ce in Y zeolite to accurately characterize their structure as prepared for sulfur adsorption.

With the addition of metals into the zeolite framework, two primary adsorption modes have been found for sulfur compounds: π-complexation and σ-bonding through direct sulfur−metal (S−M) interaction. Depending on the type of exchanged metals, either of the aforementioned adsorption modes may be favored. Transition metals including Cu^+ cations have shown strong π-complexation with thiophenic sulfur compounds due to available 4s orbitals for σ-type bonding and occupied 3d orbitals for back donation of electron density to the antibonding π-orbitals of the C═C bonds in the sulfur ring.[38−40] Similar π-complexation adsorbents have been developed with ion exchange of other transition metals.[41] Ion-exchanged rare earth metals in Y zeolite have exhibited multiple adsorption modes for thiophenic sulfur compounds including direct S−M binding and π-complexation.[42−44] In CuCeY, the combination of both adsorption modes has been credited with the high adsorption capacity and selectivity of the material.[22] In addition to the type of metals, their oxidation state plays a significant role in the desulfurization performance, with improved adsorption after reduction of the material. In particular, Cu^{2+} must be reduced to Cu^+ to allow π-complexation with sulfur compounds.[8]

Previous studies have shown X-ray absorption fine structure (XAFS) spectroscopy to be a useful method for the characterization of zeolite materials.[45−49] Specifically, Matsumoto and Tanabe used extended X-ray absorption fine structure (EXAFS) analysis of CuY during reduction with H_2 to show the formation of small metallic Cu and CuO particles.[31,33] Similar CuY materials examined with XAFS by Drake et al. and Lamberti et al. during reduction with CO showed Cu cations in the zeolite active sites[35] and the formation of small Cu metal clusters.[30] The location of Cu cations in sites I′, II′, and II is supported by XAFS, X-ray diffraction (XRD), and infrared characterization done by Turnes Palomino et al.[32] A further study by Yamashita et al. found that Cu species in Y zeolite exist as both isolated Cu^+ cations and Cu−Cu dimers.[34] In addition to the investigation of CuY, Berry et al. used EXAFS to investigate CeY materials heated *in vacuo* followed by steam treatment.[50] XAFS studies of other metals in Y zeolite have found the formation of small TiO_2 particles in the supercage[51] and Pt nanoparticles supported on the zeolite framework.[52] While XAFS has previously been used to study ion-exchanged zeolite materials, to the best of our knowledge, it has not been applied to bimetallic zeolites, including CuCeY.

Rietveld refinement of XRD data has also been used to place metal species within the framework of zeolite materials. Refinement of RE exchanged Y materials has found preference for occupation of the sodalite cages.[53,54] In bimetallic CuREY materials, the RE cations were located in the interior sites I′ and II′, while Cu was located in the supercage in site II.[36] The presence of metals in the supercage of the bimetallic Y zeolites has been suggested as a reason for their improved sulfur adsorption performance. Refinement of monometallic CuY and CeY did not show metal occupation of the supercage sites, corresponding to lower adsorption performance.[36]

To supplement experimental techniques, density functional theory (DFT) is a useful method for studying adsorptive materials. DFT calculations have been used to investigate the Cu sites in Y zeolites and examine their electronic properties.[55] Several studies have used DFT in combination with XAFS to locate exchanged ions in metal catalysts[56] and zeolites including mordenite,[57,58] zeolite X,[59] SSZ-13,[60] chabazite,[61] and zeolite Y.[35] Many studies have focused on the geometric optimization of Cu sites in particular, but less attention has been paid to Ce and other RE metals. Yu et al. reported through DFT calculations that Ce and La cations prefer the six-member ring of site I′ after geometric optimization.[62] In addition, they found closer coordination between Ce cations and O atoms near Al than with O atoms of Si−O−Si centers. Further studies have used DFT to investigate the sulfur adsorption properties of several RE exchanged NaY zeolites including CeY with the Ce cations in the six-member ring of site II.[43]

To ensure maximum sulfur adsorption capacity and selectivity, CuCeY materials are reduced prior to use for ADS. This study focuses on the characterization of CuCeY throughout the reduction process to examine the changes to the ion-exchanged Cu and Ce species imposed by the high-temperature treatment in a reducing gas environment. DFT models are optimized to create accurate representations of Cu and Ce cation sites within the zeolite framework. In situ XRD measurements of Cu and Ce exchanged Y investigate the crystalline structure of the materials after reduction. The DFT models/representations are then used as a starting point for theoretical EXAFS fitting to determine the local environment of the metals before, during, and after the reduction process. In addition, the X-ray absorption near edge structure (XANES) is analyzed to understand the changing oxidation states of the metals as they are reduced.

2. METHODS

2.1. Material Preparation. CBV 100 NaY with a Si/Al mole ratio of 2.55 was purchased from Zeolyst International as the starting material for ion exchange. Cu and Ce nitrates were used as the cation sources for the liquid phase ion exchange. The materials were exchanged to a target of 5 wt % metal. CuCeY contains approximately 2.5 wt % each of Cu and Ce, while the monometallic materials are 5 wt % of a single metal. For ion exchange of CuCeY, Ce was exchanged first followed by Cu. The metal precursors and zeolite were introduced into

https://doi.org/10.1021/acs.jpcc.1c09128
J. Phys. Chem. C 2022, 126, 1496−1512

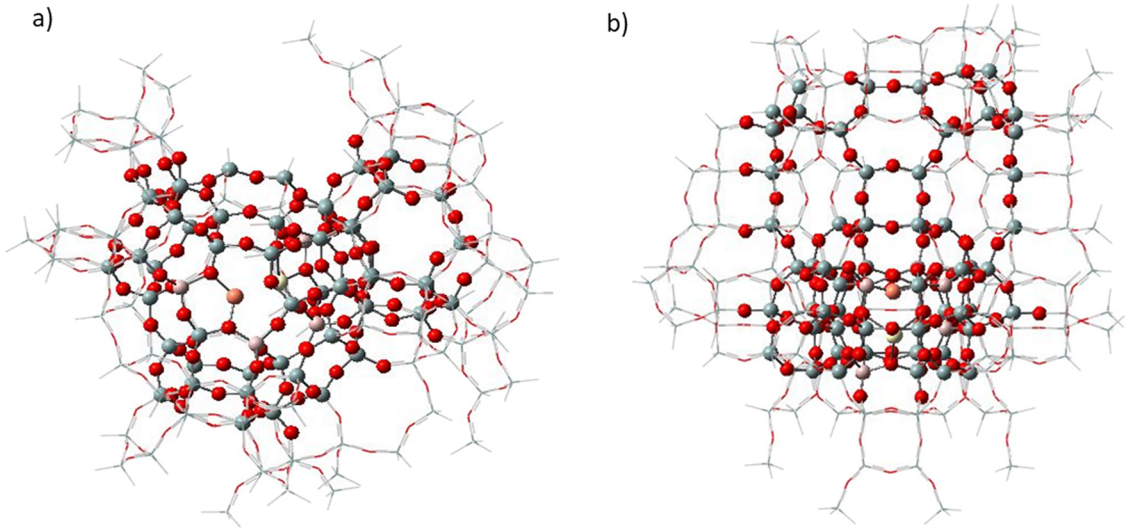

Figure 1. Top view (a) and side view (b) of the 172T ONIOM cluster model of zeolite Y showing the higher-level QM layer as ball-and-stick and the lower-level MM layer as wireframe. The active sites can be seen with Cu and Ce cations in sites II′ and I′.

an aqueous solution with approximately 100 mL of water per 1 g of zeolite and allowed to mix for 2 days to allow extensive ion exchange. The solution was found to be slightly acidic with pH 5, as expected due to the acidity of Y zeolite from to the low Si/Al ratio.[63] Following the exchange procedure, the samples were dried and calcined in air at 530 °C for 4 h. The zeolite preparation procedure is described in detail in our previous works.[18,24]

2.2. Computational Details. DFT calculations to model the placement of Cu and Ce species within the Y zeolite framework were done using the Gaussian 16 program.[64] Calculations were performed using a two-layer ONIOM model with a high-level quantum mechanics (QM) layer for atoms near the areas of high interest and active sites, and a lower-level molecular mechanics (MM) layer for the rest of the structure to decrease computation time. The QM level was used for all Cu and Ce cations as well as nearby framework O, Al, and Si atoms. This includes a total of 64 of the 172T (Si/Al) atoms in the zeolite model, leaving 108T in the MM level. Similar schemes have been employed successfully to examine Cu sites in Y[65,66] and using a three-layer QM/QM/MM model for various zeolites.[67] The ONIOM model used for the optimization of the Cu and Ce sites in Y is shown in Figure 1. The ball-and-stick components are treated at the QM level, while the wireframe shows the MM layer. The QM layer was optimized using the B3LYP functional[68,69] and the 6-31G(d,p) basis set.[70−74] The MM layer was treated with the Universal Force Field (UFF) during geometric optimizations.[75] All Ce atoms were modeled with the Stuttgart RSC 1997 effective core potential to account for the large valence of Ce.[76,77]

In building the zeolite model, an original FAU framework with only Si and O was constructed. Several sections of the Y unit cell furthest from the area of interest were omitted to decrease the required computation time, leaving the 172T subsection shown in Figure 1. Then Si atoms were exchanged for Al to control the oxidation state of the metal cations. In zeolites, framework Al atoms exist in the +3 oxidation state; thus, each Al induces a negative charge that is balanced by a position charge on the cation.[78] In this way, the desired oxidation numbers for the cations can be achieved with care to obey Löwenstein's rule and avoid Al−O−Al centers.[79] Al atoms were placed in the QM layer close to the Cu and Ce cation sites. While the Si/Al ratio of this model zeolite differs from the physical material, geometric optimization of the Cu and Ce cation sites can still be accurately achieved while controlling the oxidation state of the metal ions. The oxidation states and electronic configuration of the exchanged metals were considered in specifying the spin multiplicity of each cluster model. The models including exchanged Cu^{+} and Ce^{4+} were assigned a singlet spin state as both cations include only paired electrons, and no unpaired electrons are expected from the framework atoms. However, for models including Cu^{2+} or Ce^{3+}, the unpaired valence electrons and doublet spin state require a spin multiplicity of 2. Charge neutrality of the zeolite model was completed by capping the terminal ends with H atoms.

2.3. XRD. In situ XRD measurements were taken using a Bruker D2 Phaser diffractometer equipped with a Lynx Eye detector using Cu Kα radiation (λ = 1.54184 Å) at 40 kV and 40 mA. Measurements were performed over a 2θ range of 10−90° with a scan speed of 1.4 s/step and step size of 0.2°. For in situ reduction, samples were placed in an Anton Parr HTK1200 hot stage chamber in 3 wt % H_2 environment with balance N_2. The hot stage was heated at 10 °C/min to 450 °C and held at that temperature for 4 h. Samples were then cooled to room temperature, and a final XRD scan was taken.

2.4. XAFS Experiments. XAFS experiments were performed on the Quick X-ray Absorption and Scattering (QAS) beamline at the National Synchrotron Light Source II (NSLS-II) at Brookhaven National Laboratory. All samples were measured in fluorescence mode including the Cu K edge at 8.979 keV and Ce L-I, II, and III edges at 6.548, 6.164, and 5.723 keV, respectively. All samples were prepared as pressed pellets and placed into a Nashner−Adler cell.[80] After loading on the beamline, the cell was purged with He before the reduction procedure. For in situ reduction, 5% H_2 in He was flowed over the sample and the cell was heated to 450 °C at a rate of 10 °C/min. The temperature was held at 450 °C for 4 h and then cooled to room temperature. XAFS measurements were taken throughout the reduction cycle. For materials

https://doi.org/10.1021/acs.jpcc.1c09128
J. Phys. Chem. C 2022, 126, 1496−1512

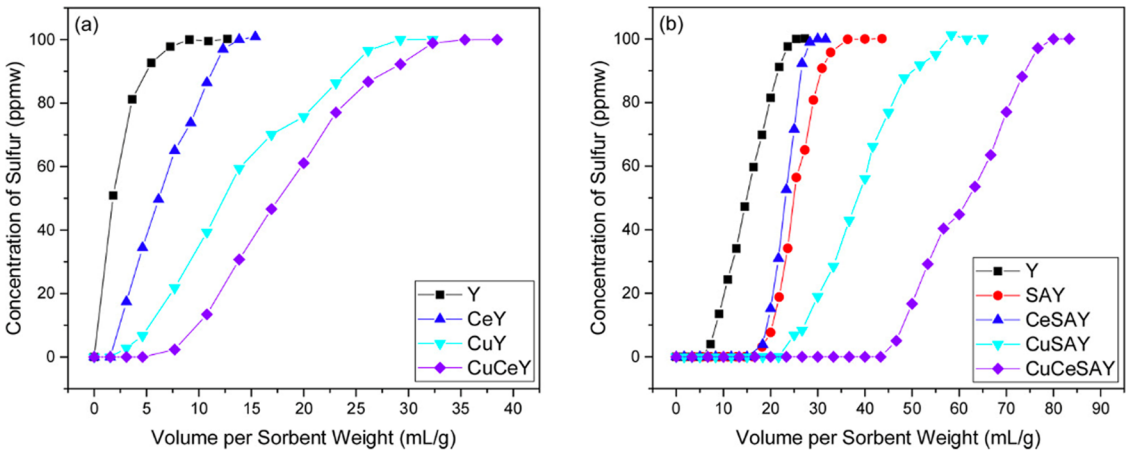

Figure 2. Breakthrough curves of Cu and Ce exchanged Y zeolites for BT (a) and DBT (b) in a 99% n-octane and 1% naphthalene model fuel. Reprinted from Lee et al.,[24] copyright 2018 with permission from Elsevier.

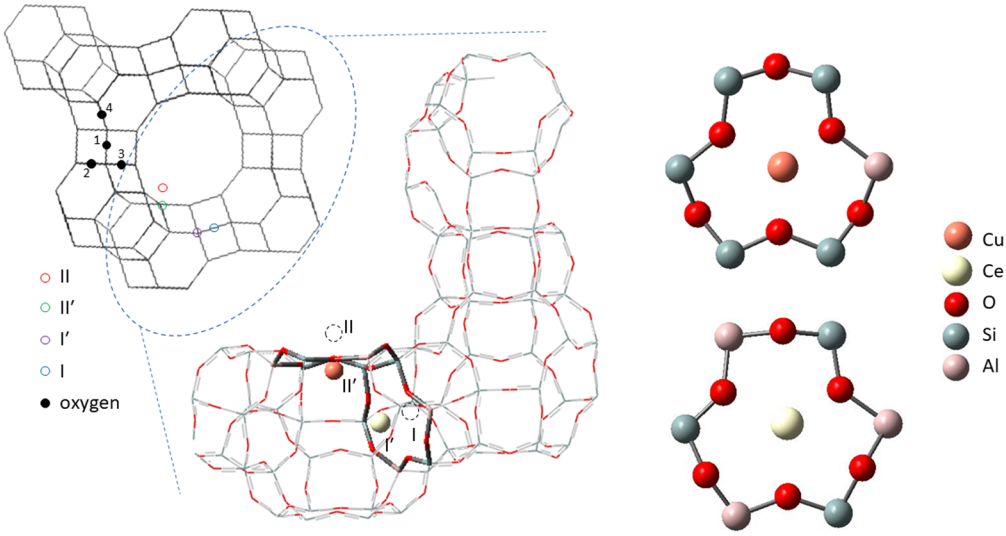

Figure 3. Cation placement within the zeolite framework with Cu^{+} located in site II′ and Ce^{3+} in site I′. The enlarged cation sites within the six-member rings show the distortion of the rings due to cation−oxygen interaction. Al atoms in the six-member rings control the oxidation number of the cations.

containing Ce, 12 scans were taken at each L edge before moving to the next edge.

Following XAFS measurements, the Demeter software package was used for data analysis.[81] The Athena program was used for processing of the raw data and analysis of the XANES region, and Artemis was used for theoretical EXAFS path fitting. Theoretical paths were generated from the DFT optimized zeolite model and known structures of Cu and Ce oxides using the FEFF code built in to the Artemis program.[82] All EXAFS path fitting was done using k^2 weighting for Fourier transforms.

3. RESULTS AND DISCUSSION

3.1. Adsorptive Desulfurization. Previously published studies by our group showing the superior sulfur adsorption of CuCeY provide the rationale behind the present work. Figure 2 shows the high capacity and selectivity of CuCeY for BT and DBT in the presence of aromatics as first reported by Lee et al.[24] While monometallic CuY and CeY exhibit improved adsorption over the parent Y, CuCeY adsorption is significantly greater than both for BT and DBT. More information and details regarding the conditions of adsorption can be found in Lee et al. (2018).[24] The objective of the current study is to elucidate the reasons behind these findings through DFT modeling and advanced spectroscopy characterization.

3.2. Computational Model. DFT calculations were used to create a model of the preferred locations of Cu and Ce cations within the zeolite framework. The metal ions were placed in the six-member rings of the zeolite including rings adjacent to the supercage and the sodalite cage, and the geometry was then optimized. Cu and Ce cations were placed within the zeolite structure according to our previous Rietveld refinement findings[36] and the known available active sites in Y zeolite.[83] A cut out of the Y unit cell is shown in Figure 3 with the positions of the cations and their local six-member rings highlighted. Calculations were performed to optimize the structures with Cu and Ce cations in sites I, I′, and II′. Single cations in site II and Cu in site I showed preference for the nearby six-member rings and migrated to site II′ and I′, respectively, during the geometric optimization. Ce in site I showed a similar local geometry related to the six-member ring

https://doi.org/10.1021/acs.jpcc.1c09128
J. Phys. Chem. C 2022, 126, 1496−1512

as in site I′, however, with increased interatomic distances and added coordination to the remaining atoms of the hexagonal prism.

The local environment of Cu and Ce in the six-member ring sites of Y including the O and average T (Si or Al) bond distances is given in Table 1. Y zeolite framework oxygen atoms have four non-equivalent positions in the unit cell structure that have been labeled 1−4 following the diagram given by Seo et al.[83] The two positions O2 and O3 are found in the six-member rings, with O2 forming an edge of two six-member rings and O3 just one. Little difference was found between the local coordination of cations found in sites I′ and II′, as both sites are located centrally in a six-member ring. However, depending on the oxidation state of the Cu cation, the coordination with nearby O atoms varies. Cu^+ shows close coordination with three O atoms at approximately 2.0 Å and a second shell with the three remaining O atoms at approximately 3.0 Å. With Cu^+ in site I′, the first shell around 2.0 Å was the O2 positions, while the farther second shell was the O3 atoms. Conversely, Cu^{2+} in the six-member ring shows significant distortion of the oxygen positions, with close coordination to four O atoms at approximately 2.0 Å including the three O2 atoms and one of the O3 atoms. The remaining two O3 atoms are found at distances just greater than 3 Å. The average Cu−T distance is around 3.1 Å for both cation oxidation states, indicating that even with Cu^{2+} distorting the positions of O atoms, the T structure of the six-member ring is relatively unperturbed and the cation is still centrally located. This is consistent with previous findings where O atoms near Al show closer coordination with exchanged cations in the six-member ring.[62] This effect is evident with Cu^+ as the shortest Cu−O distance for each O position, O2 at 1.91 Å and O3 at 2.79 Å, corresponds to O atoms next to Al in the ring structure. The same effect is seen for Cu^{2+} as oxygen of Al−O−Si positions is more closely coordinated with the cation than Si−O−Si oxygen.

Table 1. Nearest Neighbor O Bond Distances and Average Al/Si Bond Distance for Cu and Ce Located in the Six-Member Ring of Y Optimized via DFT

cation	O2 distance, Å	O3 distance, Å	Al/Si distance, Å
Cu^+	1.91, 1.98, 2.14	2.79, 3.01, 3.09	3.09
Cu^{2+}	1.89, 1.99, 2.00	2.08, 3.18, 3.35	3.16
Ce^{3+}	2.31, 2.31, 2.37	2.59, 2.63, 2.75	3.32
Ce^{4+}	2.24, 2.25, 2.25	2.57, 2.65, 2.75	3.29

Ce on the other hand prefers longer bond distances than Cu. Both Ce^{3+} and Ce^{4+} show a first coordination shell with the three O2 atoms and a longer distance to the O3 atoms when the cation is located in site II′. Ce^{3+} shows a slightly increased distance to O2 than Ce^{4+} by 0.06−0.12 Å. For both oxidation numbers, the distance to O3 is very similar, as well as the average cation to T distance. The average Ce−T distances are longer than for Cu at around 3.3 Å. This is due to the placement of the Ce cation slightly elevated out of the plane of the six-member ring and may give Ce better accessibility for adsorption by decreasing the effects of steric hindrance on the adsorption process.

The aforementioned structures generated through DFT calculations provide a useful starting point for EXAFS data fitting. Theoretical paths generated from the atomic distances and coordination near Cu and Ce are compared below to the experimental data obtained through XAFS. This will allow for the development of an accurate picture of the locations of metal species in Y zeolite before, during, and after the reduction process.

3.3. XRD. In situ XRD was used to investigate the crystalline structures of CuY, CeY, and CuCeY. The materials were subjected to the same reduction procedure as the XAFS experiments, and the XRD profiles at room temperature following the process are shown in Figure 4. The spectra show very similar patterns as the Y zeolite crystal structure is mostly preserved through ion exchange, calcination, and reduction steps. The addition of Ce into Y decreases the peak intensity, which can be observed in both CeY and CuCeY compared to CuY. The XRD profiles have been checked for significant peaks from crystalline metals and metal oxides. The dashed blue lines in Figure 4 indicated the positions of the primary peaks of fcc Cu metal at 2θ values of 43.3 and 50.4°, the primary Cu_2O peak at 36.3°, and Ce_2O_3 at 27.8°.[84] The Y zeolite samples do show a small peak near 43.3 and 27.8°; however, since these peaks are present in the spectra of parent NaY, they can be attributed to the crystalline structure of the Y zeolite framework.

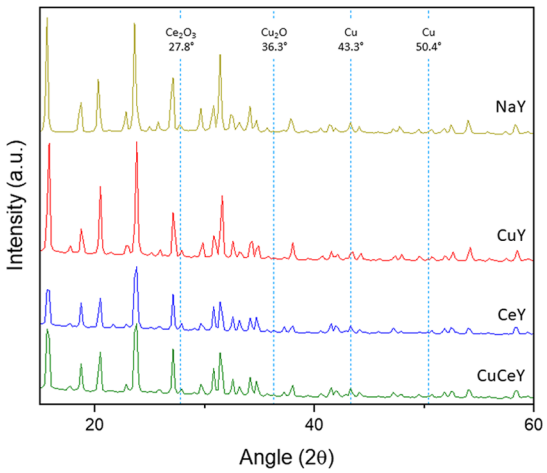

Figure 4. XRD patterns of CuY, CeY, and CuCeY after in situ reduction. Dashed vertical lines indicate the 2θ positions of primary XRD peaks in Cu^+ oxide, Ce^{3+} oxide, and metallic Cu.

In situ XRD results do not show any significant peaks from Cu or Ce metal or oxide species based on the comparison between the ion-exchanged materials and the parent NaY. This indicates that the Cu and Ce species in Y are likely present as well-dispersed and/or highly disordered structures. This finding is further justification for the use of XAFS measurements, which is the optimal technique for the study of such materials.

3.4. XAFS. Due to the sensitivity of the XAFS to local environment and oxidation state, this technique is useful for the investigation of the location and properties of metal species in zeolites. Scans done at the Cu K edge and Ce L-I, II, and III edges are utilized for examination of those metals. The XANES data will be applied to examine the oxidation states of the Cu and Ce species present in the samples during the reduction process to ensure that adequate reduction has occurred and to shed light on the active species for sulfur adsorption. Theoretical fitting of the EXAFS data will be used to probe the local environment of the Cu and Ce atoms. Due to the

https://doi.org/10.1021/acs.jpcc.1c09128
J. Phys. Chem. C 2022, 126, 1496−1512

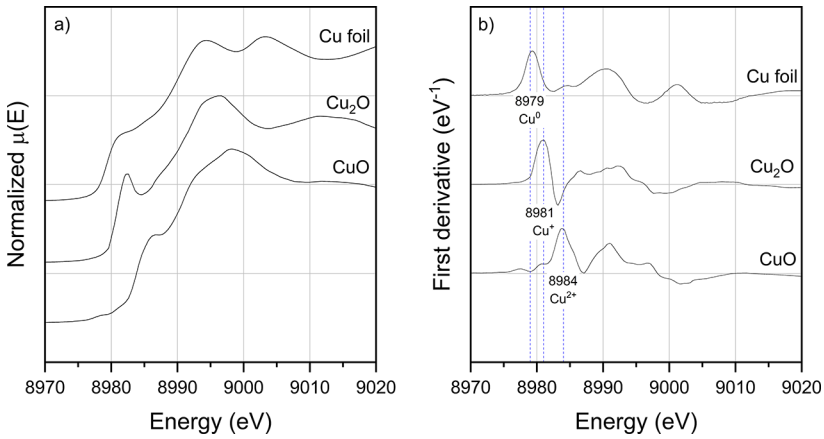

Figure 5. Normalized Cu K edge XANES of metallic and oxide Cu standards including Cu metal, Cu_2O, and CuO (a) and normalized first derivative spectra (b). Dashed lines highlight the first derivative peak locations for each sample corresponding to the 0, +1, and + 2 oxidation numbers.

complex nature of zeolite systems, the target atoms may exist in several different positions with different surrounding configurations. As previously mentioned, other studies have found exchanged metals in zeolites as cations in the active sites, as metal oxide clusters, and as metallic particles.[30−35] While the XRD results show the absence of large metal or oxide crystalline phases, there is still potential for the presence of small, well-dispersed metallic or oxide Cu and Ce. In the case where metals occupy multiple distinct environments in Y, analysis of the Cu and Ce EXAFS will attempt to identify the different phases.[85]

3.5. Standards of Ce and Cu. Several standards and precursor materials have been scanned for comparison to the XAFS spectra of the zeolite samples. These include metallic Cu, Cu_2O, and CuO for examination of Cu in the 0, +1, and +2 oxidation states. The normalized XANES signals and normalized first derivatives of these samples are shown in Figure 5. In the XANES region for these Cu standards, the well-established edge shift of a few eV to higher energy levels with increasing oxidation state is evident.[86] The Cu foil sample shows the adsorption edge beginning before 8980 eV with a prominent pre-edge shoulder around 8981 eV as is characteristic for metallic Cu.[30] The edge step for Cu_2O occurs at higher energy and is distinguished by a large peak at 8983 eV. This peak has been assigned as the 1s → 4p transition of Cu^+ cations.[87,88] In Cu_2O, this 1s → 4p feature occurs below 8985 eV for bi- and tri-coordinated Cu and above 8985 eV in tetrahedral Cu^+.[89] This peak has been found in many Cu^+ model complexes as a characteristic of the +1 state since no Cu^{2+} complex shows peaks below 8985 eV.[87] CuO shows a further increased energy of the absorption edge with a slight pre-edge feature below 8979 eV and a shoulder occurring around 8987 eV. This pre-edge feature at 8978−8979 eV has been assigned to the 1s → 3d transition.[87] With distortion of the Cu^{2+} tetrahedron, the intensity of this feature will be increased due to 4p and 3d mixing and the 8987 eV shoulder assigned to 1s → $4p_z$ will shift to a higher energy.[89] This may occur in the zeolite samples as the framework structure restricts the location of O atoms around the cation sites. These XANES features have previously been used for analysis of the oxidation states of Cu species in zeolites including faujasite,[45] ZSM-5,[90] mordenite,[45,91,92] chabazite,[92] MFI,[88] and others.[45] Additionally, the first derivative XANES data can be used to determine the oxidation state of the copper atoms present. Previous work has reported first derivative XANES maxima at 8981 and 8985 eV for Cu^+ and Cu^{2+}, respectively.[88] This difference occurs due to a shift in the peak from the 1s → 4p transition. The derivative data for the Cu standards show maximum peaks at 8979, 8981, and 8984 eV attributed to Cu^0, Cu^+, and Cu^{2+}, respectively, in agreement with the energies reported in literature. The combination of edge energy, specific XANES features, and first derivative maximum peak energy will be used for analysis of the Cu oxidation states present in the zeolite samples.

The Cu standard materials have also been examined after Fourier transform into R-space as shown in Figure 6. The

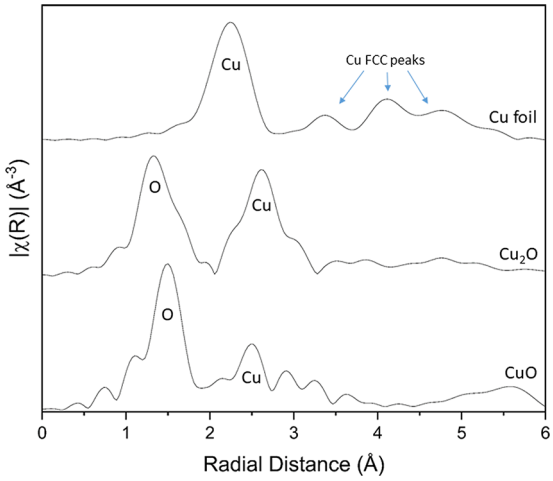

Figure 6. Fourier transform magnitudes in R-space for Cu standards including Cu metal, Cu_2O, and CuO. The scattering atoms are labeled in each corresponding peak, including the three characteristic peaks for fcc ordered Cu visible in the Cu foil sample.

EXAFS spectrum of the metallic Cu sample shows the Cu−Cu peak just after 2 Å and the three characteristic peaks of fcc ordered Cu around 3.2, 4.1, and 4.8 Å. In the two oxide samples, peaks around 1.5 and 2.5 Å are evident from Cu−O and Cu−Cu interactions. However, after 3 Å, few features are evident in the EXAFS spectra. This allows for the Cu fcc peaks to be used as clear indicators of metallic Cu−Cu interactions in the ion-exchanged zeolite samples.

https://doi.org/10.1021/acs.jpcc.1c09128
J. Phys. Chem. C 2022, 126, 1496−1512

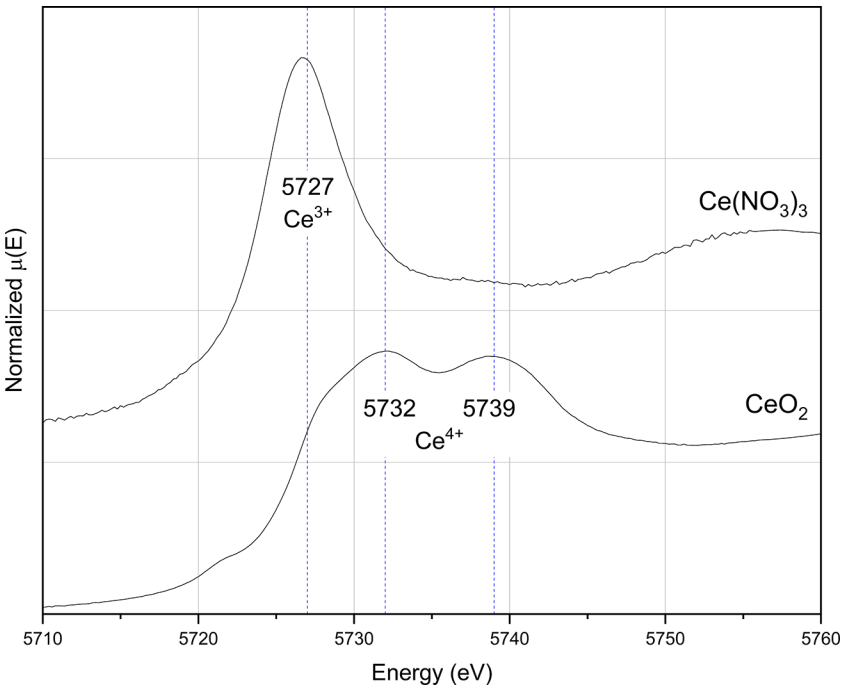

Figure 7. Normalized Ce L-III edge XANES Ce standards cerium(III) nitrate and cerium(IV) oxide. The characteristic single peak for Ce^{3+} and the double peaks for Ce^{4+} can be observed.

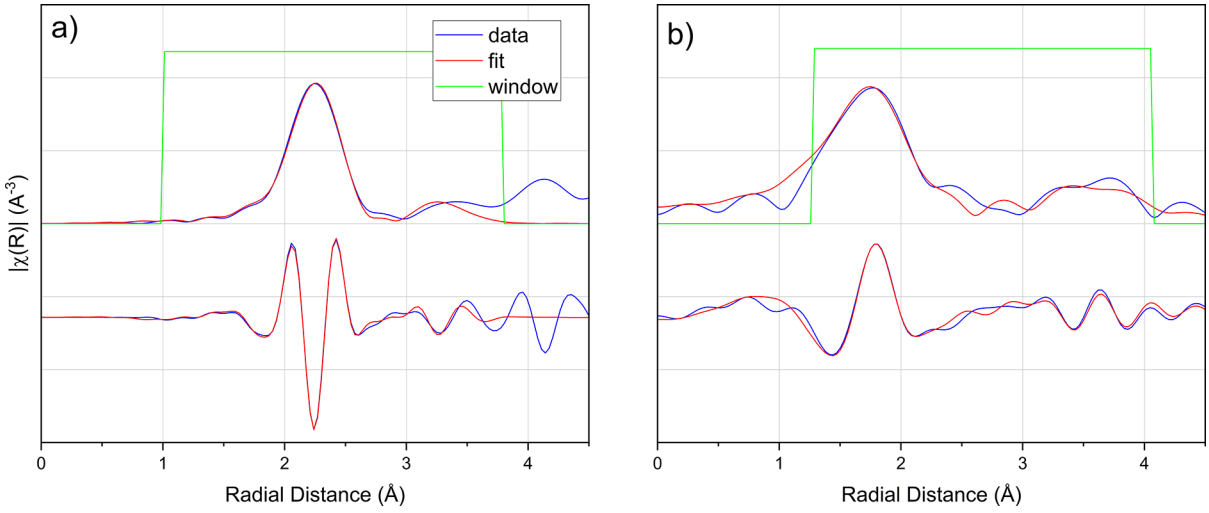

Figure 8. Theoretical EXAFS fitting to compounds with known structures: Cu foil (a) and CeO_2 (b). This fitting using constrained coordination numbers for the established crystal structure of each material allows fitting of the amplitude reduction factor, S_0^2.

In addition to Cu standards, two Ce standards have been scanned for comparison to the Ce species in the ion-exchanged zeolites as shown in Figure 7. These include $Ce(NO_3)_3$ and CeO_2 for the examination of Ce in the +3 and + 4 oxidation states, respectively. This approach has previously been used to successfully examine the reduction of Ce oxide samples.[93] From inspection of the XANES data for Ce standards at the L-III edge, there is a clear single peak at 5727 eV for Ce^{3+} and double peaks at 5732 and 5739 eV for Ce^{4+}. The 5727 eV adsorption peak in $Ce(NO_3)_3$ has been assigned to the 2p → $(4f^1)5d$ transition, while the two peaks in CeO_2 at 5732 and 5739 eV are assigned to the 2p → (4fL)5d and 2p → $(4f^0)5d$ transitions, where L is a 2p O orbital transferred to the 4f shell of Ce.[94] In addition, a small pre-edge feature can be seen in CeO_2 at 5722 eV from a 2p transition to a hybridized 4f/5d final state.[95] These characteristic peaks have been well documented in literature, and their presence will be used to determine the oxidation state of Ce species in the zeolite samples.

Before EXAFS fitting of the zeolite samples, fitting of standard materials has been used to determine the amplitude reduction factor, S_0^2. For the Cu K edge, a metallic Cu foil was used, and for the Ce L-II edge, a CeO_2 sample was used. Good fits as shown in Figure 8 with R-factor < 0.02 were obtained with a two-shell fit for Cu foil and a three-shell fit for CeO_2. These materials have well-defined crystal structures, and the known coordination numbers were used in the fitting to obtain S_0^2 values. For the metallic Cu sample with fcc structure, a first shell fitting with a N = 12 Cu−Cu single scattering path was used with a calculated path length of 2.54 Å. The second shell

https://doi.org/10.1021/acs.jpcc.1c09128
J. Phys. Chem. C 2022, 126, 1496−1512

Table 2. EXAFS Fitting Parameters for the Cu Foil and CeO_2 to Determine S_0^2 Values for Measurements at the Cu and Ce Edges

sample	scatterer	N	R, Å	ΔE_0, eV	σ^2, Å^2	S_0^2	R-factor	reduced χ^2
Cu foil	Cu	12	2.540(2)	4.5(3)	0.0085(4)	0.81(2)	0.0148	812
	Cu	6	3.57(1)		0.011(2)			
CeO_2	O	8	2.37(7)	2.3(12)	0.010(7)	0.75(5)	0.0151	318
	Ce	12	3.87(4)		0.01(1)			
	O	24	3.73(6)		0.00(0)			

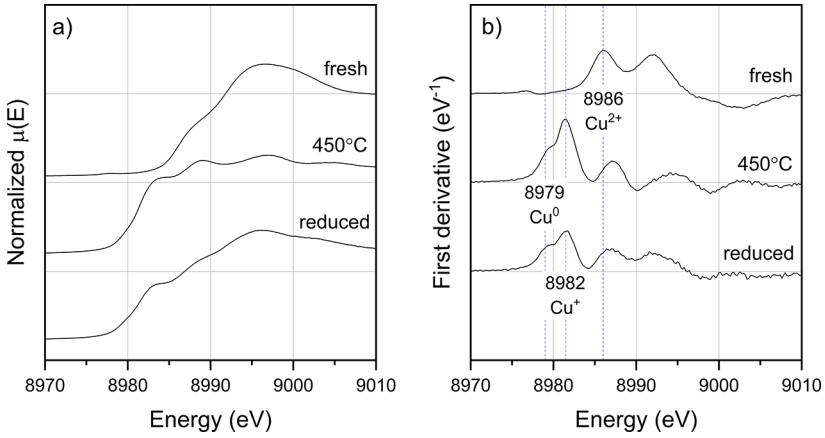

Figure 9. Cu K edge of CuY zeolite before, during, and after the reduction process showing normalized XANES spectra (a) and normalized first derivatives (b). Spectra shown include fresh CuY before reduction, CuY heated to 450 °C after 4 h, and CuY cooled to room temperature after reduction. Dashed lines indicate the locations of initial peaks in the first derivative XANES and the corresponding Cu oxidation numbers.

was a $N = 6$ Cu−Cu single scattering path at 3.57 Å. For CeO_2, two shells of single scattering paths and one double scattering path were used in the fit. These include single scattering Ce−O at 2.37 Å, single scattering Ce−Ce at 3.87 Å, and a double scattering Ce−O path at 3.73 Å with coordination numbers 8, 12, and 24, respectively. The addition of the double scattering path in the CeO_2 fitting was found to greatly increase the fit of the smaller EXAFS features, which are visible around 3 Å. The k-range and r-range used in the fits for these materials as well as the zeolite samples are given in Table S1. The best fit results are summarized in Table 2. The path lengths from theoretical path fitting are very close to the expected values from the known structures of metallic Cu and CeO_2. From the EXAFS fits of these standard materials, the S_0^2 values of 0.81 and 0.75 are calculated for fitting of the Cu K edge and Ce L-II edge, respectively. These parameters will be set for the fitting of all other samples at those edges.

3.6. XANES and EXAFS Results for CuY. To fully understand the contribution from the Cu−Ce interaction to the improved sulfur adsorption performance of CuCeY zeolites, the monometallic CuY and CeY materials were also studied for comparison. CuY with 5 wt % Cu was scanned at the Cu K edge at room temperature and continuously while heated to 450 °C, held for 4 h, and then cooled back to room temperature all while in a reducing gas environment. The XANES results for the CuY sample before, during, and after the reduction procedure are shown in Figure 9. The fresh CuY before reduction shows a similar XANES profile to the CuO standard with no prominent features occurring below 8985 eV and a slight shoulder around 8987 eV from the 1s → $4p_z$ transition, both indicators of Cu in the +2 oxidation state. When heated to 450 °C, a significant distortion of the XANES signal occurs. The edge shift to lower energy and the appearance of a peak at 8983 eV are signs of reduction to a lower oxidation state. This peak can be ascribed to the 1s → 4p transition in Cu^+; however, it appears as a shoulder rather than an independent peak as in Cu_2O due to the additional presence of Cu^{2+} features, such as the Cu^{2+} 1s → $4p_z$ peak near 8989 eV. The new edge energy below 8980 eV is consistent with Cu^0 from comparison to the Cu foil standard. These features are still evident after cooling the sample to room temperature, providing evidence for the reduction of some Cu^{2+} to Cu^+ and Cu^0 in the CuY sample.

The reduction in oxidation state can also be observed from examination of the first derivative XANES data. Before the reduction process, the first maximum derivative peak for CuY is centered at 8986 eV, corresponding to Cu in the +2 oxidation number as seen with the CuO standard. When heated to 450 °C during the reduction process, the derivative XANES data of CuY show a peak around 8982 eV with a shoulder at 8979 eV. These can be ascribed to Cu with +1 and 0 oxidation numbers, similar to the Cu_2O and metallic Cu standards. This indicates that when CuY is heated in a reducing environment, Cu^{2+} species are reduced to Cu^+ and metallic Cu^0. The same peaks in the normalized derivative XANES data can be seen after cooling the sample to room temperature, indicating the preservation of the reduced state even after cooling. These findings agree with H_2-temperature programmed reduction (TPR) studies using CuY that show the presence of two H_2 consumption peaks centered at 250 and 350 °C.[36,96] These peaks can be attributed to the reduction of Cu^{2+} species in the supercage and sodalite cages of Y, respectively, and both reductions will occur throughout the process up to 450 °C. In addition, previous work has shown that, in CuO, Cu^{2+} can be reduced directly to Cu^0, bypassing any Cu^+ intermediate states.[97] This suggests that, in CuY, any extra framework CuO may be reduced to metallic Cu, while Cu^{2+} cations are reduced to Cu^+.

https://doi.org/10.1021/acs.jpcc.1c09128
J. Phys. Chem. C 2022, 126, 1496−1512

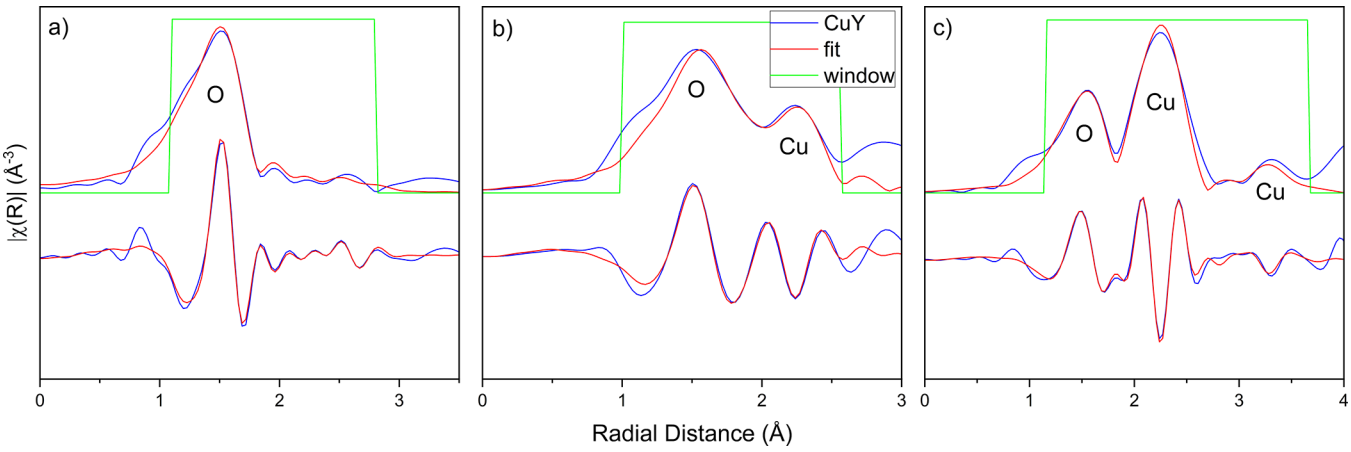

Figure 10. Comparison of the EXAFS best fit spectra to the Fourier transform magnitude and inverse Fourier transforms for CuY at the Cu K edge. Spectra shown include CuY before the reduction process (a), CuY at 450 °C at the end of the heating cycle (b), and CuY at room temperature after the reduction (c). Fits are evaluated inside of the fitting window shown in green. The scattering atoms for single scattering paths are labeled at their corresponding peaks.

To probe the local structure of the metal species within the zeolite sample, EXAFS path fitting has been done using theoretical paths from the DFT generated structures, as well as known structures of standard Cu materials. The EXAFS fitting for CuY before, during, and after the reduction process is shown in Figure 10 with the fitting parameters given in Table 3. At all points during the reduction process, there is a prominant initial peak around 1.5 Å in R-space. This feature can be attributed to Cu−O single scattering with a path length around 1.95 Å. During the heating and cooling cycles, the distance is stable, without variation outside of the uncertainty limits. This Cu−O distance is consistent with bond distances in Cu oxides, as well as Cu located in the six-member ring sites of Y. The Cu−O coordination number is less stable during the reduction process. The N value decreases from 3.8 to around 2 when the sample is reduced. The desorption of water as well as the reduction of Cu species is expected to lower the Cu−O coordination. For Cu cations in zeolites, it has been shown that one oxygen molecule is released per reduction of four Cu^{2+} cations to Cu^{+}.[98]

Table 3. Best Fit EXAFS Parameters of the k^2-Weighted Spectra for CuY during the Reduction Process at the Cu K Edge

parameter	scatterer	before	during	after
ΔE_0, eV	O	−0.6(3)	2.6(42)	2.9(6)
N		3.8(2)	1.7(7)	2.3(4)
R, Å		1.945(5)	1.98(4)	1.94(1)
σ^2, Å^2		0.0047(7)	0.010(7)	0.008(2)
ΔE_0, eV		−0.6(3)	−5.5(62)	2.2(6)
N	Cu	0.5(5)	1.3(8)	2.1(3)
R, Å		2.96(2)	2.49(4)	2.538(7)
σ^2, Å^2		0.008(7)	0.010(6)	0.006(1)
N	Cu			4.2(26)
R, Å				3.58(2)
σ^2, Å^2				0.021(8)
R-factor		0.0055	0.0051	0.0183
Reduced χ^2		50	298	37

In addition to the Cu−O path, a second shell of Cu−Cu single scattering was found to be a good fit to the experimental data. For this path, there was variation in both the path length and coordination numbers during the reduction procedure. The path length decreases from 2.96 Å in the fresh sample before treatment to around 2.5 Å when heated to 450 °C and when cooled back down to room temperature. The higher Cu−Cu scattering path length near 3 Å is consitent with the known structures of Cu oxides, while lower bond distances near 2.5 Å align with metallic Cu. The Cu−Cu coordination number is found to increase throughout the reduction process from 0.5 before reduction to 1.3 when heated to 450 °C to 2.1 when the sample was cooled back to room temperature.

A third independent path of Cu−Cu single scattering at a distance of 3.58 Å has also been included in the fit for the CuY sample after cooling to room temperature. This path contributes to fitting the characteristic Cu fcc peaks shown in the Cu foil standard sample and found in CuY after the reduction process. This is an indicator of metallic Cu clusters in the zeolite sample. As the Cu fcc peaks are not seen in the EXAFS of the sample before reduction, the high-temperature treatment must cause the assembly of metallic Cu centers in the zeolite pores.

The parameters obtained from theoretical fitting of the CuY EXAFS data as shown in Table 3 provide insight into the configuration and location of Cu species in the zeolite. Before the reduction, the scattering paths are consistent with Cu as Cu^{2+} cations within the six-member ring sites of the zeolite and oxidized Cu species in the supercage. The combination of these two Cu phases contributes to the coordination numbers and path lengths found through EXAFS fitting. The Cu−O single scattering path with a coordination number of 3.8 is close to the expected N = 4 O first shell from Cu2+ in a six-member ring site, in agreement with the optimized DFT model. The low Cu−Cu coordination of 0.5 results from singular Cu cations in the active sites and the Cu−Cu coordination of small CuO particles in the supercage. In a fully developed CuO cubic super cell, the Cu−Cu single scattering at 3 Å has a coordination number of 12. However, a fully developed crystal structure is not possible in the size constraints of the Y zeolite supercage and only small Cu oxide particles are present.

When heated to 450 °C in reducing gases, the Cu environment within CuY undergoes significant changes to both oxidation state and local configuration. EXAFS fitting of

https://doi.org/10.1021/acs.jpcc.1c09128
J. Phys. Chem. C 2022, 126, 1496−1512

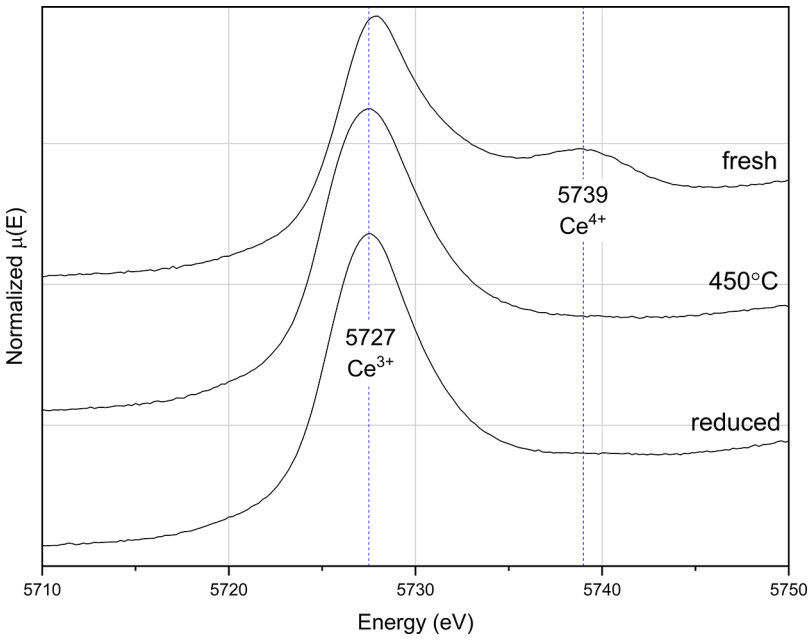

Figure 11. Normalized XANES spectra at the Ce L-III edge of CeY during the reduction processes including before reduction, at 450 °C at the end of the heating stage, and when cooled to room temperature after reduction. Dashed lines indicate the locations of significant XANES features and their corresponding Ce oxidation numbers.

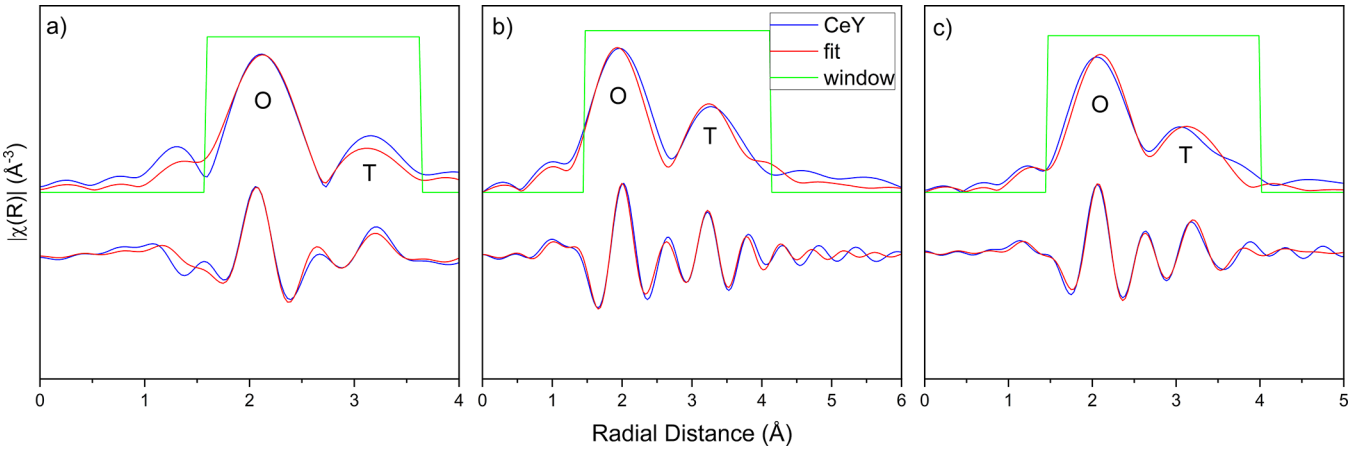

Figure 12. EXAFS fitting of CeY at the Ce L-II edge showing "best fit" in red compared to the Fourier transform magnitude and inverse Fourier transform. CeY before the reduction process (a), CeY at 450 °C at the end of the heating cycle (b), and CeY at room temperature after reduction (c) all show similar EXAFS features. Scattering atoms from best fit single scattering paths are labeled at their respective peak locations.

the Cu−O indicates the reduction of Cu oxides in the supercage to metallic Cu and reduction of Cu^{2+} cations in six-member ring sites I′ and II′ to Cu^{+}. This is supported by the XANES results showing the reduction of Cu^{2+} to Cu^{+} and Cu^{0}, as well as the changes in the EXAFS Cu−Cu single scattering path fitting. In the room temperature sample after reduction, the Cu−Cu path length has decreased to 2.54 Å, consistent with the shorter interatomic distances of metallic Cu rather than Cu oxides. In addition, the characteristic Cu fcc peaks are visible in the EXAFS spectrum of CuY at room temperature after reduction, indicating the formation of metal clusters. However, the Cu−Cu coordination number around 2 indicates that only small metallic Cu particles are present.

XANES data and EXAFS fitting results for CuY suggest that, after ion exchange and calcination, Cu exists as Cu^{2+} cations within the zeolite active sites I′ and II′ as well as some oxidized Cu in the pores of the zeolite. After reduction and subsequent cooling to room temperature, Cu^{2+} cations are reduced to Cu^{+}, while supercage Cu forms small metallic Cu^{0} clusters. The formation of Cu metal clusters in Y zeolite has been previously reported after reduction of CuY with CO.[30,33] It is possible that both Cu configurations can contribute to the adsorption of sulfur compounds.

3.7. XANES and EXAFS Results in CeY. XAFS measurements done at the Ce L-I, II, and III edges were used to analyze CeY during the reduction process. The Ce L-III edge data were used for XANES analysis, while the L-II edge was used for EXAFS path fitting. The XANES data in Figure 11 show that the untreated sample has both Ce^{3+} and Ce^{4+} oxidation states due to the signature +3 peak around 5727 eV and the smaller second peak at 5739 eV from the +4 state. The other characteristec peak of Ce^{4+} at 5732 eV is not visible due to the prominence of the 5727 eV feature. When the sample is heated to 450 °C, it is evident that the Ce is reduced

https://doi.org/10.1021/acs.jpcc.1c09128
J. Phys. Chem. C 2022, 126, 1496−1512

to the +3 state due to the dissappearance of the peak at 5739 eV, and this remains after cooling back to room temperature. This result is in agreement with previous research showing a singular peak in CeY H_2-TPR corresponding to the reduction of surface and supercage Ce^{4+} to Ce^{3+}.[42]

Analysis of the EXAFS spectra at the Ce L-II edge was used in addition to the XANES data to probe the local environment of Ce in the CeY sample. Figure 12 shows the EXAFS fitting of the fresh zeolite before reduction, at 450 °C, and at room temperature after the reduction. Unlike CuY, the EXAFS profiles of CeY throughout the process are largely similar, with some slight distortion during the reduction process. The k^2-weighted Fourier transforms show a first peak around 2 Å in R-space and a second smaller peak just after 3 Å.

Initial fitting of the CeY EXAFS data was performed using single scattering paths based on the zeolite model obtained through DFT. The resulting parameters are given in Table 4.

Table 4. Best Fit EXAFS Parameters of the k^2-Weighted Spectra for CeY during the Reduction Process at the Ce L-II Edge

parameter	scatterer	before	during	after
ΔE_0, eV		10.7(5)	6.6(4)	9.1(3)
N	O	6.9(5)	8.5(6)	9.3(6)
R, Å		2.61(4)	2.52(2)	2.59(5)
σ^2, Å^2		0.007(9)	0.017(4)	0.013(9)
N	Si/Al	3.9(10)	3.5(26)	3.4(6)
R, Å		3.52(3)	3.48(6)	3.48(2)
σ^2, Å^2		0.009(13)	0.03(1)	0.005(8)
N	Si/Al		4.19(25)	5.9(16)
R, Å			4.03(2)	4.11(4)
σ^2, Å^2			0.00(1)	0.01(1)
R-factor		0.0231	0.0234	0.0164
reduced χ^2		59	62	31

The first peak was fit using a single scattering Ce−O path at a distance of around 2.5−2.6 Å. The second peak just after 3 Å was fit with a Ce−T scattering path as EXAFS path fitting cannot easily differentiate between Si and Al backscatterering, so it is convenient to include both atoms in this single theoretical path. In addition, the nature of the zeolite material makes it difficult to ascertain the exact number of Al and Si in each six-member ring. When the sample was heated to 450 °C and after cooling to room temperature, two distinct paths were found to contribute to the second peak around 3 Å. These were fit using distinct Ce−T paths with different radial distances near 3.5 and 4 Å. The similarity in path length of these two scatterers leads to their appearance as a singular peak in the EXAFS spectra.

The findings from theoretical fitting of the EXAFS data are consistent with Ce cations located in the active sites of Y, including the six-member ring sites I′ and II′ and the hexagonal prism site I. The Ce−O bond distances are similar to those expected from DFT calculations, and the increasing coordination number of the Ce−O path during reduction is evidence for Ce migration into the hexagonal prisms. In site I, the expected Ce−O coordination is 12, so a combination of Ce in that site as well as the six-member ring sites can account for the N value of 9.3 after CeY has been reduced and cooled to room temperature. This same effect can be seen in the Ce−T path fitting. Before reduction, the best fit results from a single Ce−T path at 3.5 Å. This distance is in agreement with the DFT calculated distances between Ce in the six-member ring and adjacent framework Si and Al. When the reduction process begins, the addition of a second Ce−T path around 4 Å is found to improve the fit to the data. This longer scattering distance is consistent with Ce located in site I, as the central location in the hexagonal prism results in larger distances to the framework atoms. This is evidence of the migration of Ce cations into the interior site of Y during the reduction process. However, the low coordination number near $N = 6$ suggests that a significant portion of Ce remains in the six-member ring sites. Overall, XAFS results for CeY show that Ce cations are exchanged into the active sites of Y and reduction converts Ce^{4+} to Ce^{3+} while driving the cations further into the interior sites of Y, including site I. This conclusion is supported by previous work locating Ce species in the interior ion exchange postions of the Y framework.[50,54,99]

3.8. XANES and EXAFS Results on Cu in CuCeY. Now that the structure of exchanged metals in the monometallic CuY and CeY is better understood, XAFS experiments to examine the bimetallic CuCeY will shed light on how the two metals interact with each other in Y zeolite. The Cu K edge XANES in Figure 13 shows a similar pattern to the reduction of Cu in monometallic CuY. Initally, Cu in the fresh CuCeY is

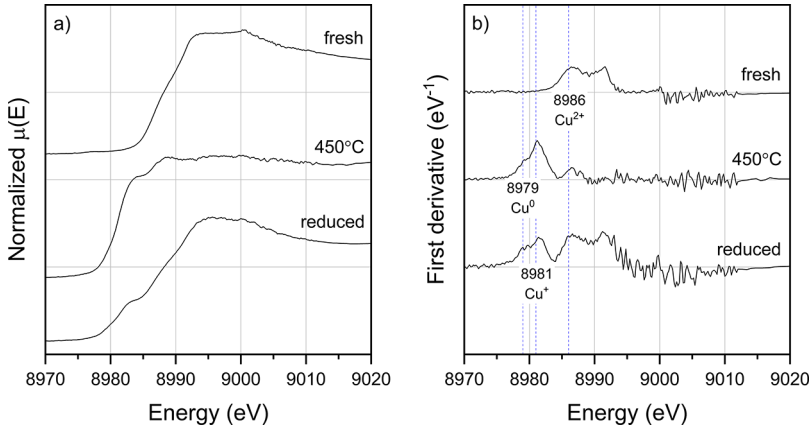

Figure 13. Cu K edge of CuCeY zeolite before, during, and after the reduction process showing normalized XANES spectra (a) and normalized first derivative (b). Spectra shown include from top to bottom: fresh CuCeY before reduction, CuCeY at 450 °C at the end of the heating process, and CuCeY cooled to room temperature after reduction.

https://doi.org/10.1021/acs.jpcc.1c09128
J. Phys. Chem. C 2022, 126, 1496−1512

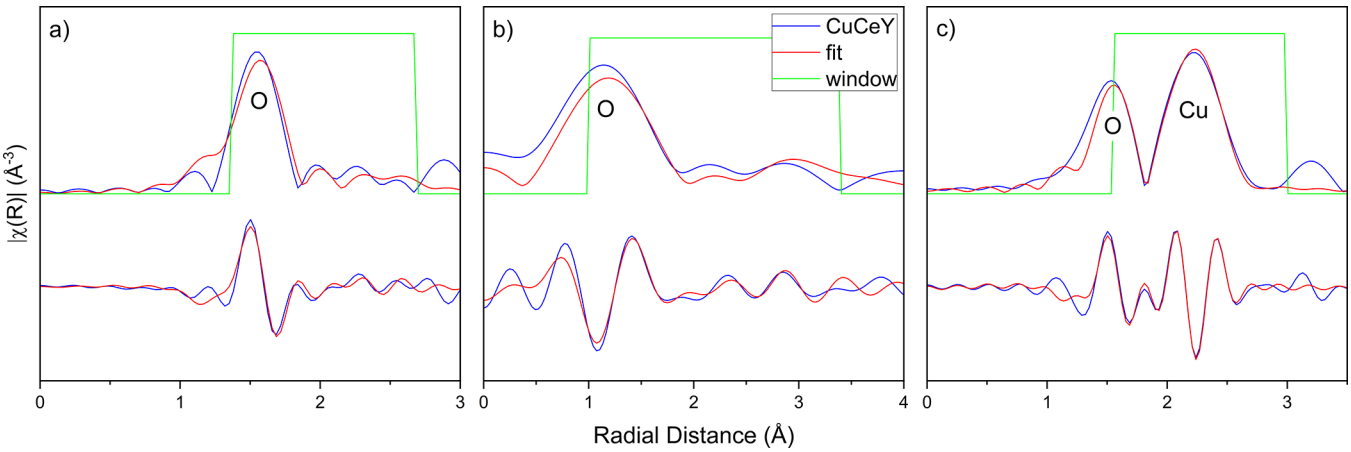

Figure 14. EXAFS fitting of CuCeY at the Cu K edge showing "best fit" in red compared to the Fourier transform magnitude and real part of the inverse Fourier transform. Fresh CuCeY before the reduction process (a), CuCeY during reduction at 450 °C (b), and CuCeY at room temperature after reduction (c) are shown. Scattering atoms for the best fit single scattering paths are labeled.

in the +2 oxidation state. The XANES profile of fresh CuCeY is similar to that of CuO with an edge step after 8985 eV and a shoulder near 8987 eV from the 1s → $4p_z$ transition, both features providing evidence of Cu in the +2 oxidation state. Upon heating to 450 °C in the reducing environment, there is significant distortion of the XANES spectra including an edge shift to lower energy and emergence of a peak around 8983 eV. This peak was seen with Cu_2O and has been assigned to the 1s → 4p transition of Cu^+. When cooled to room temperature, the intensity of the Cu^+ and Cu^{2+} features at 8983 and 8987 eV is somewhat lessened. This evidence for the reduction of Cu^{2+} is also apparent from the first derivative XANES data. The edge shift to lower energy levels can be cleary seen from the initial peaks in the derivative data. The fresh CuCeY samples have an initial first derivative peak at 8986 eV, consistent with Cu^{2+}. When heated, lower energy peaks at 8979 and 8981 eV appear and can be attributed to Cu^0 and Cu^+, respectively.

EXAFS fitting of the Cu K edge data for CuCeY was done using a two-shell fitting approach. Theoretical fitting paths were based on the structures from DFT as well as known structures of Cu standard materials. As can be seen in the EXAFS data given in Figure 14, there is significant distortion of the Cu local environment during the reduction process. In addition, after reduction and cooling to room temperature, the EXAFS data show the characteristic Cu fcc peaks, indicating the formation of some metallic Cu in CuCeY, as was found with CuY.

EXAFS data for both fresh CuCeY and room temperature CuCeY after the reduction show a first shell in R-space around 1.5 Å. When the samples were heated at 450 °C, this peak shifted to a slightly shorter radial distance just over 1 Å. In all cases, this peak has been fit by a Cu−O single scattering path. The fitting parameters are given in Table 5 and show the path lengths and coordination numbers for the theoretical paths used in the fitting. For the Cu−O path, the distance decreases slightly when heated but returns near to the original length after cooling to room temperature. This may be due to the distortion of the structure at high temperature and mobility of the Cu atoms during reduction. The final distance after cooling just below 2 Å is consistent with Cu cations located in the six-member ring sites of Y. The Cu−O coordination number decreases from 1.7 in the fresh samples to 1.0 after reduction. This is consistent with the expected loss of oxygen from

Table 5. Best Fit EXAFS Parameters of the k^2-weighted Spectra for CuCeY during the Reduction Process at the Cu K Edge

parameter	scatterer	before	during	after
ΔE_0, eV	O	8.2(7)	−7.5(55)	4.2(17)
N	O	1.7(1)	1.0(7)	1.0(1)
R, Å		1.956(2)	1.82(5)	1.933(9)
σ^2, Å^2		0.003(2)	0.02(1)	0.000(1)
ΔE_0, eV	Cu			2.0(7)
N	Cu			1.47(9)
R, Å				2.530(8)
σ^2, Å^2				0.005(1)
R-factor		0.0240	0.0193	0.0198
reduced χ^2		225	119	492

dehydration of the material and reduction of oxide species. The N = 1 value of the reduced CuCeY sample is lower than the N = 2.3 that was found in CuY, which may indicate a greater proportion of Cu as metallic Cu rather than as cations in the zeolite sites. This finding supports the expected occupancy of some sites by Ce, reducing the number available for Cu.

In addition to the first shell Cu−O path, a second shell of Cu−Cu single scattering has been included in the EXAFS fitting of the reduced sample after cooling to room temperature. The path length around 2.5 Å is consistent with the expected Cu−Cu distances found in metallic Cu. This appearance of a Cu−Cu single scattering path is similar to what was seen in CuY and can be taken as an indicator of the formation of metallic Cu clusters. The final coordination number near N = 1.5 suggests a limited Cu cluster size of only a few atoms. This indicates that metallic Cu exists as either Cu dimers or trimers rather than large particles, likely due to size limitations within zeolite pore structure.

XAFS analysis of the Cu species in CuCeY shows the reduction of Cu^{2+} to Cu^+ and metallic Cu particles. This is supported by XANES data showing evidence of the reduced oxidation states and EXAFS path fitting with Cu−O and Cu−Cu single scattering paths. The EXAFS findings support a greater proportion of Cu as metallic Cu in the zeolite pores than in the cation form as compared to the monometallic CuY. This agrees with previous findings showing that in bimetallic

https://doi.org/10.1021/acs.jpcc.1c09128
J. Phys. Chem. C 2022, 126, 1496−1512

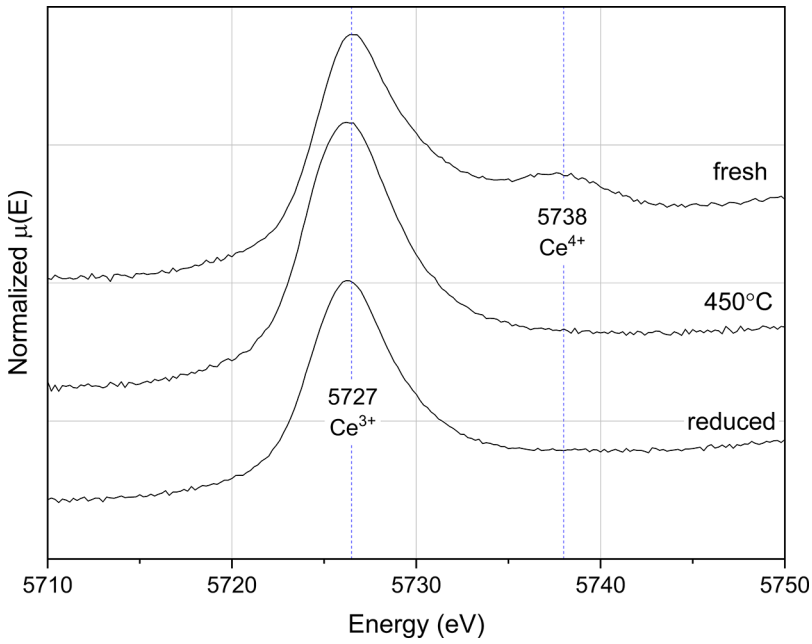

Figure 15. Normalized XANES spectra at the Ce L-III edge of CuCeY during the reduction processes including before reduction, at 450 °C at the end of the heating stage, and when cooled to room temperature after reduction. Dashed lines indicate the peak locations corresponding to Ce in the +3 and +4 oxidation states.

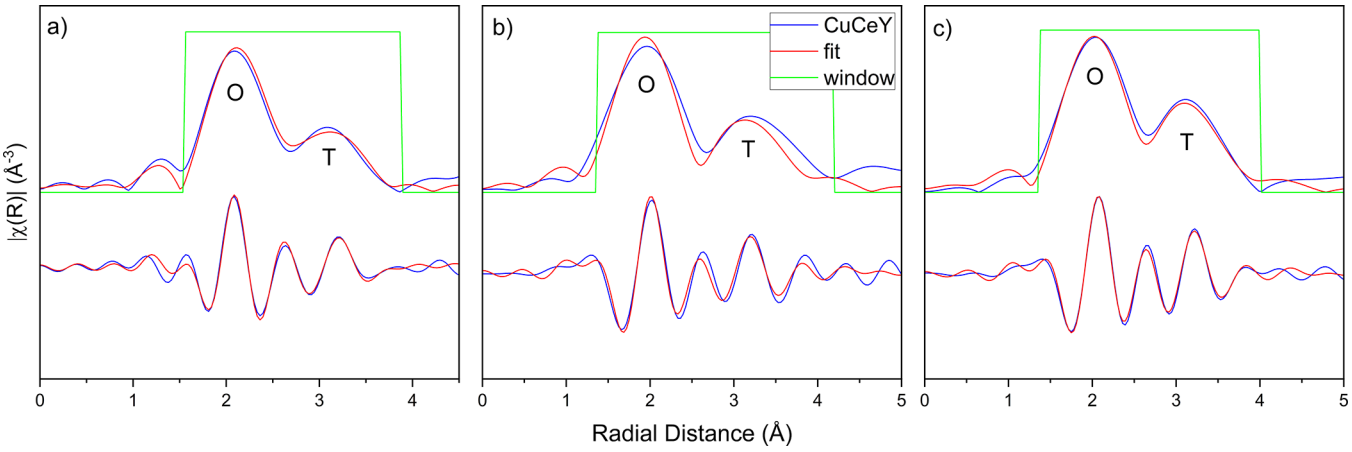

Figure 16. EXAFS fitting of CuCeY at the Ce L-II edge showing "best fit" in red compared to the Fourier transform magnitude and the real part of the inverse Fourier transform. EXAFS fitting of fresh CuCeY before the reduction process (a), CuCeY at 450 °C during the reduction (b), and CuCeY at room temperature after reduction (c) show similar features.

zeolites with Cu and RE metals, Cu preferentially occupies the external sites close to the supercage.[36] Likely, the addition of Ce into the interior sites of Y prevents the maximum exchange of Cu cations into sites I′ and II′.

3.9. XANES and EXAFS on Ce in CuCeY. CuCeY has also been investigated through XAFS measurements at the Ce L edges. XANES data at the Ce L-III edge given in Figure 15 show a similar reduction of Ce as observed in CeY. The XANES features of the fresh sample indicate the prescence of Ce as both +3 and +4 oxidation states due to the presence of peaks at both 5727 and 5738 eV. During the reduction process, the peak at 5738 eV from Ce^{4+} disappears, indicating complete reduction to the +3 oxidation state.

The EXAFS features at the Ce L-II edge of CuCeY also show similarities to CeY. As can be seen in Figure 16, the EXAFS shows two primary peaks throughout the reduction process. The first peak shows the greatest intensity and is centered on 2 Å. A second smaller peak can be seen just after 3 Å. These peaks have been fit by a single scattering Ce−O path and two single scattering Ce−T paths with fitting parameters given in Table 6. Throughout the reduction procedure, there is little variation in the visible EXAFS features at the Ce edge in CuCeY, although the fitting parameters reveal subtle changes in the Ce environment.

The EXAFS placement of the Ce species in CuCeY is in good agreement with the expected location of Ce cations from DFT structural optimization as the bond distances for Ce−O and Ce−T paths are close to the calculated values. The Ce−O distance around 2.5−2.6 Å is consistent with the range of distances in the DFT model. The first Ce−T path around 2.5 Å is similar to the expected distance with Ce in the six-member ring of Y. The second Ce−T path near 4 Å fits the DFT model of Ce in the hexagonal prism site I. There is little variation in the Ce−T paths throughout the reduction process, suggesting

https://doi.org/10.1021/acs.jpcc.1c09128
J. Phys. Chem. C 2022, 126, 1496−1512

Table 6. Best Fit EXAFS Parameters of the k^2-Weighted Spectra for CuCeY during the Reduction Process at the Ce L-III Edge

parameter	scatterer	before	during	after
ΔE_0, eV		9.0(3)	5.7(5)	6.4(3)
N	O	5.6(4)	7.8(5)	8.0(16)
R, Å		2.60(5)	2.50(8)	2.56(6)
σ^2, Å^2		0.005(3)	0.012(8)	0.01(1)
N	Si/Al	2.9(4)	2.4(22)	3.0(10)
R, Å		3.51(2)	3.45(8)	3.46(6)
σ^2, Å^2		0.003(2)	0.02(2)	0.013(6)
N	Si/Al	12.4(28)	10.9(24)	11.7(15)
R, Å		4.14(6)	4.02(4)	4.07(4)
σ^2, Å^2		0.031(6)	0.016(5)	0.011(3)
R-factor		0.0110	0.0310	0.0072
reduced χ^2		4.0	4.0	3.7

that, in CuCeY, the Ce cations have occupied site I during the calcination step prior to reduction. However, the increasing Ce−O coordination numbers during the heating process can be ascribed to some further movement of Ce cations in the hexagonal prism of site I. This is significant as, in CeY, there was no indication of Ce occupancy of site I prior to reduction. This difference may be attributed to the interactions between Cu and Ce during ion exchange and the preferential occupation of exterior sites by Cu, driving Ce into the more interior sites.

XAFS analysis of CuCeY at both Cu and Ce edges gives a complete picture of the zeolite after it has been reduced for optimal sulfur adsorption performance. It is found that Ce occupies the internal zeolite sites including sites I, I′, and potentially II′ as Ce^{3+} cations. Cu has been found in the more external sites of Y close to the supercage including I′ and II′ as well as in small metallic Cu dimers or trimers in the supercage itself. Due to similarities between sites I′ and II′, they cannot be easily distinguished when locating Ce and Cu cations. These results agree with the proposed DFT model of ion-exchanged Y zeolite. The DFT model has accurately predicted the affinity of Ce cations for the hexagonal prism site I and both Cu and Ce cations for the six-member ring sites I′ and II′. The bond distances between metal cations and nearby atoms and their coordination numbers are in good agreement between the DFT model and EXAFS fitting results. Due to the novelty of finding metallic Cu species in the zeolite framework, this structure was not included in the DFT model and may be investigated in further work.

4. CONCLUSIONS

This study used several methods for the characterization of Cu and Ce active sites in Y zeolite during the in situ reduction process for sulfur adsorption. XANES analysis of CuY, CeY, and CuCeY samples shows the reduction of Ce^{4+} to Ce^{3+} and Cu^{2+} to Cu^{+} and metallic Cu^0. EXAFS path fitting has been used to place the Cu and Ce species within the zeolite samples. Ce cations are found to prefer the interior sites of Y within the hexagonal prism and the six-member rings after reduction, corresponding to sites I, I′, and II′ in the Y framework. Since sites I′ and II′ share the same local structure and cannot be easily differentiated, Ce may occupy only the more internal I′ or both sites. Additionally, Ce in CuCeY is found in site I prior to reduction, while Ce in CeY only occupies that site after heating to 450 °C, indicating interaction between Cu and Ce species during ion exchange. Conversely, Cu tends to occupy more external sites including Cu^{+} cations in the six-member ring sites and well-dispersed metallic Cu dimer or trimer particles. While the preferential locations of each metal in the monometallic and bimetallic zeolites are similar, changes in the site occupancy can explain the superior sulfur adsorption of CuCeY. Compared to CuY, Cu in CuCeY indicates a larger fraction of Cu species as metallic Cu particles rather than cations in the active sites of Y. This can be ascribed to interactions between Cu and Ce and the occupation of interior sites by Ce. The dispersion of small metallic Cu clusters may increase the number of available adsorption sites in CuCeY and improve adsorption performance. In our previous experimental studies, this arrangement of Cu and Ce in CuCeY has shown exceptional adsorption performance.[36] When compared to monometallic CuY and CeY, as well as other CuREY, the increased occupancy of site II by Cu when paired with Ce led to greater adsorption capacity for both BT and DBT. Overall, in CuCeY, both metals can occupy sites accessible to large sulfur compounds in the supercage, giving CuCeY materials both high sulfur capacity and selectivity.

■ ASSOCIATED CONTENT

Supporting Information

The Supporting Information is available free of charge at https://pubs.acs.org/doi/10.1021/acs.jpcc.1c09128.

The k-range and r-range used for theoretical EXAFS fitting of Cu and Ce samples (Table S1) (PDF)

■ AUTHOR INFORMATION

Corresponding Authors

Anatoly I. Frenkel − *Stony Brook University, Stony Brook, New York 11794, United States;* orcid.org/0000-0002-5451-1207; Email: anatoly.frenkel@stonybrook.edu

Julia A. Valla − *University of Connecticut, Storrs, Connecticut 06269, United States;* orcid.org/0000-0002-4402-0818; Phone: +1 (860) 486 0583; Email: ioulia.valla@uconn.edu

Authors

Henry J. Sokol − *University of Connecticut, Storrs, Connecticut 06269, United States*

Amani M. Ebrahim − *Stony Brook University, Stony Brook, New York 11794, United States;* orcid.org/0000-0001-9979-2586

Stavros Caratzoulas − *University of Delaware, Newark, Delaware 19716, United States;* orcid.org/0000-0001-9599-4199

Complete contact information is available at: https://pubs.acs.org/10.1021/acs.jpcc.1c09128

Notes

The authors declare no competing financial interest.

■ ACKNOWLEDGMENTS

The research was funded in part by the NSF CAREER Award #1844767 and Advanced Manufacturing for Energy Systems (AMES) fellowship at the University of Connecticut, funded by US Department of Energy Advanced Manufacturing Office traineeship program, grant DE-EE0008302. S.C. and A.I.F. acknowledge support by the Catalysis Center for Energy Innovation, an Energy Frontier Research Center funded by the

US Department of Energy, Office of Science, Office of Basic Energy Sciences, under award DE-SC0001004. This research used beamline 7-BM (QAS) of the National Synchrotron Light Source II, a U.S. DOE Office of Science User Facility operated for the DOE Office of Science by Brookhaven National Laboratory under contract DE-SC0012704. Beamline operations were supported in part by the Synchrotron Catalysis Consortium (U.S. DOE, Office of Basic Energy Sciences, grant DE-SC0012335). We thank Drs. S. Ehrlich, L. Ma, and N. Marinkovic for help with the in situ measurements at the QAS beamline.

■ ABBREVIATIONS

XRD, X-ray diffraction; XAFS, X-ray adsorption fine structure; DFT, density functional theory; HDS, hydrodesulfurization; ADS, adsorptive desulfurization; FAU, faujasite; RE, rare earth; BT, benzothiophene; DBT, dibenzothiophene; 4,6-DMDBT, 4,6-dimethyldibenzohiophene; EXAFS, extended X-ray adsorption fine structure; XANES, X-ray adsorption near edge structure; QM, quantum mechanics; MM, molecular mechanics; UFF, Universal Force Field; NSLS-II, National Synchrotron Light Source II; TPR, temperature programmed reduction

■ REFERENCES

(1) Aydın, H.; İlkılıç, C. Air Pollution, Pollutant Emissions and Harmfull Effects. *J. Eng. Technol.* **2017**, *1*, 8−15.

(2) Jafarinejad, S. Control and Treatment of Sulfur Compounds Specially Sulfur Oxides (SOx) Emissions from the Petroleum Industry: A Review. *Chem. Int.* **2016**, *2*, 242−253.

(3) Valla, J. A.; Mouriki, E.; Lappas, A. A.; Vasalos, I. A. The Effect of Heavy Aromatic Sulfur Compounds on Sulfur in Cracked Naphtha. *Catal. Today* **2007**, *127*, 92−98.

(4) *Control of Air Pollution from New Motor Vehicles: Heavy-Duty Engine and Vehicle Standards and Highway Diesel Sulfur Control Requirements*; US Environmental Protection Agency: Washington, DC, 2001; Vol. *66*.

(5) *Control of Emissions of Air Pollution From Diesel Fuel*; US Environmental Protection Agency: Washington, DC, 2005; Vol. *70*.

(6) *Control of Air Pollution From Motor Vehicles: Tier 3 Motor Vehicle Emission and Fuel Standards*; US Environmental Protection Agency: Washington, DC, 2014; Vol. *79*.

(7) Babich, I. V.; Moulijn, J. a. Science and Technology of Novel Processes for Deep Desulfurization of Oil Refinery Streams: A Review. *Fuel* **2003**, *82*, 607−631.

(8) Wang, Y.; Yang, F. H.; Yang, R. T.; Heinzel, J. M.; Nickens, A. D. Desulfurization of High-Sulfur Jet Fuel by π-Complexation with Copper and Palladium Halide Sorbents. *Ind. Eng. Chem. Res.* **2006**, *45*, 7649−7655.

(9) Song, C. An Overview of New Approaches to Deep Desulfurization for Ultra-Clean Gasoline, Diesel Fuel and Jet Fuel. *Catal. Today* **2003**, *86*, 211−263.

(10) Velu, S.; Ma, X.; Song, C. Selective Adsorption for Removing Sulfur from Jet Fuel over Zeolite-Based Adsorbents. *Ind. Eng. Chem. Res.* **2003**, *42*, 5293−5304.

(11) Lee, K. X.; Valla, J. A. Adsorptive Desulfurization of Liquid Hydrocarbons Using Zeolite-Based Sorbents: A Comprehensive Review. *React. Chem. Eng.* **2019**, *4*, 1357−1386.

(12) Crandall, B. S.; Zhang, J.; Stavila, V.; Allendorf, M. D.; Li, Z. Desulfurization of Liquid Hydrocarbon Fuels with Microporous and Mesoporous Materials: Metal-Organic Frameworks, Zeolites, and Mesoporous Silicas. *Ind. Eng. Chem. Res.* **2019**, *58*, 19322−19352.

(13) Ma, X.; Velu, S.; Kim, J. H.; Song, C. Deep Desulfurization of Gasoline by Selective Adsorption over Solid Adsorbents and Impact of Analytical Methods on Ppm-Level Sulfur Quantification for Fuel Cell Applications. *Appl. Catal. B Environ.* **2005**, *56*, 137−147.

(14) Yang, R. T.; Hernández-Maldonado, A. J.; Yang, F. H. Desulfurization of Transportation Fuels with Zeolites under Ambient Conditions. *Science* **2003**, *301*, 79−81.

(15) Lutz, W.; Zeolite, Y. Synthesis, Modification, and Properties-A Case Revisited. *Adv. Mater. Sci. Eng.* **2014**, *2014*, 1−20.

(16) Ward, J. W. The Nature of Active Sites on Zeolites I. The Decationated Y Zeolite. *J. Catal.* **1967**, *9*, 225−236.

(17) Xiao, J.; Li, Z.; Liu, B.; Xia, Q.; Yu, M. Adsorption of Benzothiophene and Dibenzothiophene on Ion-Impregnated Activated Carbons and Ion-Exchanged Y Zeolites. *Energy Fuels* **2008**, *22*, 3858−3863.

(18) Lee, K. X.; Valla, J. A. Investigation of Metal-Exchanged Mesoporous Y Zeolites for the Adsorptive Desulfurization of Liquid Fuels. *Appl. Catal. B Environ.* **2017**, *201*, 359−369.

(19) Song, H.; Chang, Y.; Song, H. Deep Adsorptive Desulfurization over Cu, Ce Bimetal Ion-Exchanged Y-Typed Molecule Sieve. *Adsorption* **2016**, *22*, 139−150.

(20) Lee, K. X.; Wang, H.; Karakalos, S.; Tsilomelekis, G.; Valla, J. A. Adsorptive Desulfurization of 4,6-Dimethyldibenzothiophene on Bimetallic Mesoporous y Zeolites: Effects of Cu and Ce Composition and Configuration. *Ind. Eng. Chem. Res.* **2019**, *58*, 18301−18312.

(21) Shan, J. H.; Liu, X. Q.; Sun, L. B.; Cui, R. Cu-Ce Bimetal Ion-Exchanged Y Zeolites for Selective Adsorption of Thiophenic Sulfur. *Energy Fuels* **2008**, *22*, 3955−3959.

(22) Song, H.; Song, H.; Wan, X.; Dai, M.; Zhang, J.; Li, F. Deep Desulfurization of Model Gasoline by Selective Adsorption over Cu-Ce Bimetal Ion-Exchanged y Zeolite. *Fuel Process. Technol.* **2013**, *116*, 52−62.

(23) Zu, Y.; Guo, Z.; Zheng, J.; Hui, Y.; Wang, S.; Qin, Y.; Zhang, L.; Liu, H.; Gao, X.; Song, L. Investigation of Cu(I)-Y Zeolites with Different Cu/Al Ratios towards the Ultra-Deep Adsorption Desulfurization: Discrimination and Role of the Specific Adsorption Active Sites. *Chem. Eng. J.* **2020**, *380*, 122319.

(24) Lee, K. X.; Tsilomelekis, G.; Valla, J. A. Removal of Benzothiophene and Dibenzothiophene from Hydrocarbon Fuels Using CuCe Mesoporous Y Zeolites in the Presence of Aromatics. *Appl. Catal. B Environ.* **2018**, *234*, 130−142.

(25) Botana-de la Cruz, A.; Boahene, P. E.; Vedachalam, S.; Dalai, A. K.; Adjaye, J. Mesoporous Adsorbents for Desulfurization of Model Diesel Fuel: Optimization, Kinetic, and Thermodynamic Studies. *Fuels* **2020**, *1*, 47−58.

(26) Yoosuk, B.; Silajan, A.; Prasassarakich, P. Deep Adsorptive Desulfurization over Ion-Exchanged Zeolites: Individual and Simultaneous Effect of Aromatic and Nitrogen Compounds. *J. Cleaner Prod.* **2020**, *248*, 119291.

(27) Cerutti, M.; Hackbarth, F.; Maass, D.; Chiaro, S.; Pinto, R.; Cardoso, M.; Arroyo, P.; Ulson de Souza, A.; de Souza, S. Copper-Exchanged Y Zeolites for Gasoline Deep-Desulfurization. *Adsorption* **2019**, *25*, 1595−1609.

(28) Kosinov, N.; Liu, C.; Hensen, E. J. M.; Pidko, E. A. Engineering of Transition Metal Catalysts Confined in Zeolites. *Chem. Mater.* **2018**, *30*, 3177−3198.

(29) Berthomieu, D.; Delahay, G. Recent Advances in CuI/IIY: Experiments and Modeling. *Catal. Rev. - Sci. Eng.* **2006**, *48*, 269−313.

(30) Lamberti, C.; Spoto, G.; Scarano, D.; Pazé, C.; Salvalaggio, M.; Bordiga, S.; Zecchina, A.; Palomino, G. T.; D'Acapito, F. CuI-Y and CuII-Y Zeolites: A XANES, EXAFS and Visible-NIR Study. *Chem. Phys. Lett.* **1997**, *269*, 500−508.

(31) Tanabe, S.; Matsumoto, H. Activation Process of CuY Zeolite Catalyst Observed by TPR and EXAFS Measurements. *Bull. Chem. Soc. Jpn.* **1990**, *63*, 192−198.

(32) Turnes Palomino, G.; Bordiga, S.; Zecchina, A.; Marra, G. L.; Lamberti, C. XRD, XAS, and IR Characterization of Copper-Exchanged Y Zeolite. *J. Phys. Chem. B* **2000**, *104*, 8641−8651.

(33) Matsumoto, H.; Tanabe, S. Catalytic Behavior and Structure of Active Species of Cu-Y Zeolite in Oxidation of Carbon Monoxide. *J. Phys. Chem.* **1990**, *94*, 4207−4212.

(34) Yamashita, H.; Matsuoka, M.; Tsuji, K.; Shioya, Y.; Anpo, M.; Che, M. In-Situ XAFS, Photoluminescence, and IR Investigations of

Copper Ions Included within Various Kinds of Zeolites. Structure of Cu(I) Ions and Their Interaction with CO Molecules. *J. Phys. Chem.* **1996**, *100*, 397−402.
(35) Drake, I. J.; Zhang, Y.; Briggs, D.; Lim, B.; Chau, T.; Bell, A. T. The Local Environment of Cu+ in Cu-Y Zeolite and Its Relationship to the Synthesis of Dimethyl Carbonate. *J. Phys. Chem. B* **2006**, *110*, 11654−11664.
(36) Lee, K. X.; Crowl, T. B.; Sokol, H. J.; Morales-acosta, M. D.; Valla, J. A. Understanding the Role of Rare Earths in Zeolite Y on the Removal of Sulfur from Hydrocarbon Fuels. *J. Phys. Chem. C* **2021**, *125*, 9107−9118.
(37) Zu, Y.; Hui, Y.; Qin, Y.; Zhang, L.; Liu, H.; Zhang, X.; Guo, Z.; Song, L.; Gao, X. Facile Fabrication of Effective Cerium(III) Hydroxylated Species as Adsorption Active Sites in CeY Zeolite Adsorbents towards Ultra-Deep Desulfurization. *Chem. Eng. J.* **2019**, *375*, 122014.
(38) Hernández-Maldonado, A. J.; Yang, R. T. Desulfurization of Diesel Fuels by Adsorption via π-Complexation with Vapor-Phase Exchanged Cu(I)-Y Zeolites. *J. Am. Chem. Soc.* **2004**, *126*, 992−993.
(39) Song, X. L.; Sun, L. B.; He, G. S.; Liu, X. Q. Isolated Cu(I) Sites Supported on β-Cyclodextrin: An Efficient π-Complexation Adsorbent for Thiophene Capture. *Chem. Commun.* **2011**, *47*, 650−652.
(40) Hernández-Maldonado, A. J.; Yang, R. T. New Sorbents for Desulfurization of Diesel Fuels via π-Complexation. *AIChE J.* **2004**, *50*, 791−801.
(41) Hernández-Maldonado, A. J.; Yang, F. H.; Qi, G.; Yang, R. T. Desulfurization of Transportation Fuels by π-Complexation Sorbents: Cu(I)-, Ni(II)-, and Zn(II)-Zeolites. *Appl. Catal. B Environ.* **2005**, *56*, 111−126.
(42) Mo, Z.; Qin, Y.; Zu, Y.; Wang, H.; Zhang, X.; Song, L. Effect of Content of Cerium Ion on Brönsted-Acid-Catalyzed Reaction of Thiophene over CeY Zeolite Studied by In Situ FTIR Spectroscopy. *ChemistrySelect* **2019**, *4*, 13034−13044.
(43) Gao, X.; Geng, W.; Zhang, H.; Zhao, X.; Yao, X. Thiophenic Compounds Adsorption on Na(I)Y and Rare Earth Exchanged y Zeolites: A Density Functional Theory Study. *J. Mol. Model.* **2013**, *19*, 4789−4795.
(44) Wang, L.; Sun, Z.; Ding, Y.; Chen, Y.; Li, Q.; Xu, M.; Li, H.; Song, L. A Theoretical Study of Thiophenic Compounds Adsorption on Cation-Exchanged y Zeolites. *Appl. Surf. Sci.* **2011**, *257*, 7539−7544.
(45) Sushkevich, V. L.; Safonova, O. V.; Palagin, D.; Newton, M. A.; van Bokhoven, J. A. Structure of Copper Sites in Zeolites Examined by Fourier and Wavelet Transform Analysis of EXAFS. *Chem. Sci.* **2020**, *11*, 5299−5312.
(46) Agostini, G.; Lamberti, C.; Palin, L.; Milanesio, M.; Danilina, N.; Xu, B.; Janousch, M.; Van Bokhoven, J. A. In Situ XAS and XRPD Parametric Rietveld Refinement to Understand Dealumination of Y Zeolite Catalyst. *J. Am. Chem. Soc.* **2010**, *132*, 667−678.
(47) Joyner, R. W.; Sonntag, O.; Smith, A. D.; Stockenhuber, M. A Soft X-Ray EXAFS Study of the Variation of the Local Aluminium Structure on Adsorption of Bases in Various Zeolite Types. *Stud. Surf. Sci. Catal.* **2007**, 756−761.
(48) Shido, T.; Yamaguchi, A.; Inada, Y.; Asakura, K.; Nomura, M.; Iwasawa, Y. Dispersive XAFS Study on Cu and Mo Species in Zeolites during the Catalyst Preparation. *Top. Catal.* **2002**, *18*, 53−58.
(49) Salama, T. M.; Shido, T.; Ohnishi, R.; Ichikawa, M. EXAFS/XANES, XRD, and UV-Vis Characterization of Intrazeolitic Gold(I) Prepared by Monolayer Dispersion of AuCl 3 inside Na-Y Zeolite. *J. Phys. Chem.* **1996**, *100*, 3688−3694.
(50) Berry, F. J.; Marco, J. F.; Steel, A. T. An Investigation by EXAFS of the Thermal Dehydration and Rehydration of Cerium- and Erbium-Exchanged Y-Zeolite. *J. Alloys Compd.* **1993**, *194*, 167−172.
(51) Schultz, E.; Ferrini, C.; Prins, R. Exafs and Xanes on Ti-Containing Zeolite Y. *Jpn. J. Appl. Phys.* **1993**, *32*, 490−492.
(52) Li, Z.; Yan, W.; Wei, S. XAFS Study of HY Zeolite Supported Pt Nanoparticle Catalysts Prepared with Different Methods. *AIP Conf. Proc.* **2007**, *882*, 714−717.
(53) Qiu, L.; Fu, Y.; Zheng, J.; Huang, N.; Lu, L.; Gao, X.; Xin, M.; Luo, Y.; Shi, Y.; Xu, G. Investigation on the Cation Location, Structure and Performances of Rare Earth-Exchanged Y Zeolite. *J. Rare Earths* **2017**, *35*, 658−666.
(54) Nery, J. G.; Mascarenhas, Y. P.; Bonagamba, T. J.; Mello, N. C.; Souza-Aguiar, E. F. Location of Cerium and Lanthanum Cations in CeNaY and LaNaY after Calcination. *Zeolites* **1997**, *18*, 44−49.
(55) Berthomieu, D.; Krishnamurty, S.; Coq, B.; Delahay, G.; Goursot, A. Theoretical Modeling of a Copper Site in a Cu(II) - Y Zeolite. *J. Phys. Chem. B* **2001**, *105*, 1149−1156.
(56) Moon, J. S.; Kim, E. G.; Lee, Y. K. Active Sites of Ni2P/SiO2 Catalyst for Hydrodeoxygenation of Guaiacol: A Joint XAFS and DFT Study. *J. Catal.* **2014**, *311*, 144−152.
(57) Buono, C.; Martini, A.; Pankin, I. A.; Pappas, D. K.; Negri, C.; Kvande, K.; Lomachenko, K. A.; Borfecchia, E. Local Structure of Cu(I) Ions in the MOR Zeolite: A DFT-Assisted XAS Study. *Radiat. Phys. Chem.* **2020**, *175*, 108111.
(58) Lamberti, C.; Bordiga, S.; Zecchina, A.; Salvalaggio, M.; Geobaldo, F.; Otero Areán, C. XANES, EXAFS and FTIR Characterization of Copper-Exchanged Mordenite. *J. Chem. Soc. - Faraday Trans.* **1998**, *94*, 1519−1525.
(59) Guesmi, H.; Massiani, P. A Combined EXAFS and DFT Study of the Ni2+ Environment in Dehydrated Ni/NaX. *Catal. Today* **2011**, *177*, 25−30.
(60) Paolucci, C.; Parekh, A. A.; Khurana, I.; Di Iorio, J. R.; Li, H.; Albarracin Caballero, J. D.; Shih, A. J.; Anggara, T.; Delgass, W. N.; Miller, J. T.; et al. Catalysis in a Cage: Condition-Dependent Speciation and Dynamics of Exchanged Cu Cations in Ssz-13 Zeolites. *J. Am. Chem. Soc.* **2016**, *138*, 6028−6048.
(61) Pankin, I. A.; Martini, A.; Lomachenko, K. A.; Soldatov, A. V.; Bordiga, S.; Borfecchia, E. Identifying Cu-Oxo Species in Cu-Zeolites by XAS: A Theoretical Survey by DFT-Assisted XANES Simulation and EXAFS Wavelet Transform. *Catal. Today* **2020**, *345*, 125−135.
(62) Yu, S.; Tian, H.; Dai, Z.; Zhu, Y.; Long, J. Different Influences of Lanthanum and Cerium on Stability of y Zeolite and Their DFT Calculations. *China Pet. Process. Petrochemical Technol.* **2011**, *13*, 16−23.
(63) Lohse, U.; Parlitz, B.; Patzelova, V. Y Zeolite Acidity Dependence on the Si/Al Ratio. *J. Phys. Chem.* **1989**, *93*, 3677−3683.
(64) Frisch, M. J.; Trucks, G. W.; Schlegel, H. B.; Scuseria, G. E.; Robb, M. A.; Cheeseman, J. R.; Scalmani, G.; Barone, V.; Petersson, G. A.; Nakatsuji, H. et al. *Gaussian 16*. Gaussian, Inc.: Wallingford, CT 2016.
(65) Archipov, T.; Santra, S.; Ene, A. B.; Stoll, H.; Rauhut, G.; Roduner, E. Adsorption of Benzene to Copper in CuHY Zeolite. *J. Phys. Chem. C* **2009**, *113*, 4107−4116.
(66) Santra, S.; Archipov, T.; Ene, A. B.; Komnik, H.; Stoll, H.; Roduner, E.; Rauhut, G. Adsorption of Dioxygen to Copper in CuHY Zeolite. *Phys. Chem. Chem. Phys.* **2009**, *11*, 8855−8866.
(67) Patet, R. E.; Caratzoulas, S.; Vlachos, D. G. Adsorption in Zeolites Using Mechanically Embedded ONIOM Clusters. *Phys. Chem. Chem. Phys.* **2016**, *18*, 26094−26106.
(68) Becke, A. D. A New Mixing of Hartree-Fock and Local Density-Functional Theories. *J. Chem. Phys.* **1993**, *98*, 1372−1377.
(69) Lee, C.; Yang, W.; Parr, R. G. Developement of the Colle-Salvetti Correlation-Energy Formula into a Functional of the Electron Density. *Phys. Rev. B* **1988**, *37*, 785−789.
(70) Rassolov, V. A.; Pople, J. A.; Ratner, M. A.; Windus, T. L. 6-31G* Basis Set for Atoms K through Zn. *J. Chem. Phys.* **1998**, *109*, 1223−1229.
(71) Hariharan, P. C.; Pople, J. A. The Influence of Polarization Function on Molecular Orbital Hydrogenation Energies. *Theor. Chim. Acta* **1973**, *28*, 213.
(72) Hehre, W. J.; Ditchfield, R.; Pople, J. A. Self — Consistent Molecular Orbital Methods. XII. Further Extensions of Gaussian — Type Basis Sets for Use in Molecular Orbital Studies of Organic Molecules. *J. Chem. Phys.* **1972**, *56*, 2257−2261.
(73) Francl, M. M.; Pietro, W. J.; Hehre, W. J.; Binkley, J. S.; Gordon, M. S.; DeFrees, D. J.; Pople, J. A. Self-Consistent Molecular

https://doi.org/10.1021/acs.jpcc.1c09128
J. Phys. Chem. C 2022, 126, 1496−1512

Orbital Methods. XXIII. A Polarization-Type Basis Set for Second-Row Elements. *J. Chem. Phys.* **1982**, *77*, 3654−3665.
(74) Gordon, M. S.; Binkley, J. S.; Pople, J. A.; Pietro, W. J.; Hehre, W. J. Self-Consistent Molecular-Orbital Methods. 22. Split-Valence Basis Sets for Second-Row Elements. *J. Am. Chem. Soc.* **1982**, *104*, 2797−2803.
(75) Rappé, A. K.; Casewit, C. J.; Colwell, K. S.; Goddard, W. A.; Skiff, W. M. UFF, a Full Periodic Table Force Field for Molecular Mechanics and Molecular Dynamics Simulations. *J. Am. Chem. Soc.* **1992**, *114*, 10024−10035.
(76) Dolg, M.; Preuss, H. Energy-Adjusted Ab Initio Pseudopotentials for the Rare Earth Elements. *J. Chem. Phys.* **1989**, *90*, 1730−1734.
(77) Pritchard, B. P.; Altarawy, D.; Didier, B.; Gibson, T. D.; Windus, T. L. New Basis Set Exchange: An Open, Up-to-Date Resource for the Molecular Sciences Community. *J. Chem. Inf. Model.* **2019**, *59*, 4814−4820.
(78) Ravi, M.; Sushkevich, V. L.; van Bokhoven, J. A. Towards a Better Understanding of Lewis Acidic Aluminium in Zeolites. *Nat. Mater.* **2020**, *19*, 1047−1056.
(79) Loewenstein, W. The Distribution of Aluminum in the Tetrahedra of Silicates and Aluminates. *Am. Mineral.* **1954**, *39*, 92−96.
(80) Marinkovic, N. S.; Ehrlich, S. N.; Northrup, P.; Chu, Y.; Frenkel, A. I. Synchrotron Catalysis Consortium (SCC) at NSLS-II: Dedicated Beamline Facilities for In Situ and Operando Characterization of Catalysts. *Synchrotron Radiat. News* **2020**, *33*, 4−9.
(81) Ravel, B.; Newville, M. ATHENA, ARTEMIS, HEPHAESTUS: Data Analysis for X-Ray Absorption Spectroscopy Using IFEFFIT. *J. Synchrotron Radiat.* **2005**, *12*, 537−541.
(82) Newville, M. IFEFFIT: Interactive XAFS Analysis and FEFF Fitting. *J. Synchrotron Radiat.* **2001**, *8*, 322−324.
(83) Seo, S. M.; Kim, H. S.; Chung, D. Y.; Suh, J. M.; Lim, W. T. The Effect of Co2+-Ion Exchange Time into Zeolite y (FAU, Si/Al = 1.56): Their Single-Crystal Structures. *Bull. Korean Chem. Soc.* **2014**, *35*, 243−249.
(84) Jain, A.; Ong, S. P.; Hautier, G.; Chen, W.; Richards, W. D.; Dacek, S.; Cholia, S.; Gunter, D.; Skinner, D.; Ceder, G. The Materials Project: A Materials Genome Approach to Accelerating Materials Innovation. *APL Mater.* **2013**, *1*, xxx.
(85) Kunquan, L.; Jun, W. Extended X-Ray-Absorption Fine Structure of a System of Mixed Phases. *Phys. Rev. B* **1987**, *35*, 4497−4499.
(86) Gaur, A.; Shrivastava, D.; Joshi, K. Copper K-Edge XANES of Cu(I) and Cu(II) Oxide Mixtures. *J. Phys. Conf. Ser.* **2009**, *190*, 0−4.
(87) Kau, L. S.; Spira-solomon, D. J.; Penner-hahn, J. E.; Hodgson, K. O.; Solomon, E. I. X-Ray Absorption Edge Determination of the Oxidation State and Coordination Number of Copper: Application to the Type 3 Site in Rhus Vernicifera Laccase and Its Reaction with Oxygen. *J. Am. Chem. Soc.* **1987**, *109*, 6433−6442.
(88) Lamberti, C.; Bordiga, S.; Bonino, F.; Prestipino, C.; Berlier, G.; Capello, L.; D'Acapito, F.; Llabrés, I.; Xamena, F. X.; Zecchina, A. Determination of the Oxidation and Coordination State of Copper on Different Cu-Based Catalysts by XANES Spectroscopy in Situ or in Operando Conditions. *Phys. Chem. Chem. Phys.* **2003**, *5*, 4502−4509.
(89) Kau, L. S.; Hodgson, K. O.; Solomon, E. I. X-Ray Absorption Edge and Exafs Study of the Copper Sites in Zno Methanol Synthesis Catalysts. *J. Am. Chem. Soc.* **1989**, *111*, 7103−7109.
(90) Kumashiro, R.; Kuroda, Y.; Nagao, M. New Analysis of Oxidation State and Coordination Environment of Copper Ion-Exchanged in ZSM-5 Zeolite. *J. Phys. Chem. B* **1999**, *103*, 89−96.
(91) Lee, I.; Lee, M.-S.; Tao, L.; Ikuno, T.; Khare, R.; Jentys, A.; Huthwelker, T.; Borca, C. N.; Kalinko, A.; Gutiérrez, O. Y.; et al. Activity of Cu−Al−Oxo Extra-Framework Clusters for Selective Methane Oxidation on Cu-Exchanged Zeolites. *JACS Au* **2021**, *1*, 1412−1421.
(92) Borfecchia, E.; Pappas, D. K.; Dyballa, M.; Lomachenko, K. A.; Negri, C.; Signorile, M.; Berlier, G. Evolution of Active Sites during Selective Oxidation of Methane to Methanol over Cu-CHA and Cu-MOR Zeolites as Monitored by Operando XAS. *Catal. Today* **2019**, *333*, 17−27.
(93) Ukawa, T.; Nishide, K.; Yamamoto, Y.; Yamashita, S.; Katayama, M.; Inada, Y. XAFS Analysis on Reduction Process of Cerium Oxide. *Mem. SR Cent. Ritsumeikan Univ.* **2019**, *20*, 5−8.
(94) Zhang, J.; Wu, Z.; Liu, T.; Hu, T.; Wu, Z.; Ju, X. XANES Study on the Valence Transitions in Cerium Oxide Nanoparticles. *J. Synchrotron Radiat.* **2001**, *8*, 531−532.
(95) Akahashi, Y. O. T.; Himizu, H. I. S.; Sui, A. K. U.; Agi, H. I. K.; Omura, M. A. N. Direct Observation of Tetravalent Cerium in Ferromanganese Nodules and Crusts by X-Ray-Adsorption near-Edge Structure (XANES). *Geochim. Cosmochim. Acta* **2000**, *64*, 2929−2935.
(96) Iwamto, M.; Ohura, S.; Furukawa, H.; Nagano, H.; Kagawa, S. Reduction Mechanism of Copper Ions Exchanged in y Type Zeolites. *Reports Fac. Eng.* **1982**, *18*, 89−92.
(97) Kim, J. Y.; Rodriguez, J. A.; Hanson, J. C.; Frenkel, A. I.; Lee, P. L. Reduction of CuO and Cu2O with H2: H Embedding and Kinetic Effects in the Formation of Suboxides. *J. Am. Chem. Soc.* **2003**, *125*, 10684−10692.
(98) Sushkevich, V. L.; Smirnov, A. V.; Van Bokhoven, J. A. Autoreduction of Copper in Zeolites: Role of Topology, Si/Al Ratio, and Copper Loading. *J. Phys. Chem. C* **2019**, *123*, 9926−9934.
(99) Garcia, F. A. C.; Araújo, D. R.; Silva, J. C. M.; De Macedo, J. L.; Ghesti, G. F.; Dias, S. C. L.; Dias, J. A.; Filho, G. N. R. Effect of Cerium Loading on Structure and Morphology of Modified Ce-USY Zeolites. *J. Braz. Chem. Soc.* **2011**, *22*, 1894−1902.

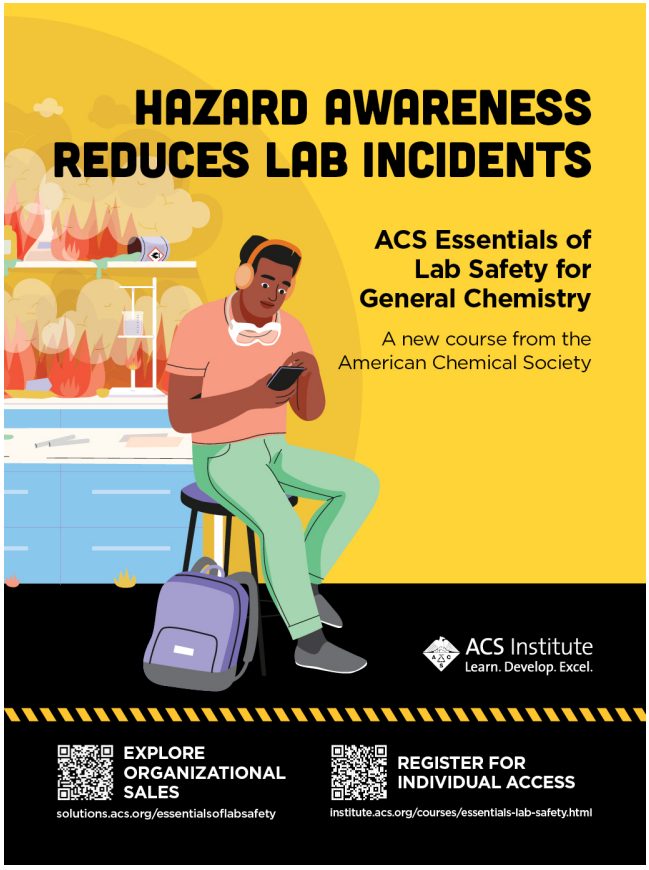

https://doi.org/10.1021/acs.jpcc.1c09128
J. Phys. Chem. C 2022, 126, 1496−1512